

Acoustic instability prediction of the flow through a circular aperture in a thick plate via an impedance criterion

J. Sierra-Ausin^{1,2}, D. Fabre¹, V. Citro² and F. Giannetti^{2,†}

¹Institut de Mécanique des Fluides de Toulouse (IMFT), Université de Toulouse, CNRS, Toulouse 31400, France

²Dipartimento di Ingegneria (DIIN), Università degli Studi di Salerno, Fisciano 84084, Italy

(Received 20 August 2021; revised 20 April 2022; accepted 25 April 2022)

We investigate the mechanisms leading to acoustic whistling for a jet passing through a circular hole in a thick plate connecting two domains. Two generic situations are considered. In the first one, the upstream domain is a closed cavity while the downstream domain is open, leading to a class of conditionally unstable modes. In this case, the instability source lies in the recirculation region within the thickness of the plate, but coupling with a conveniently tuned resonator is needed to select the conditional instability range. In the second situation, the two regions, upstream and downstream of the hole, are considered as open, leading to a class of hydrodynamic modes where instability of the recirculation region is sufficient to generate self-oscillations without the need of any resonator. A matched asymptotic model, valid in the low Mach limit, is used to derive a global impedance of the system, combining the impedance of the hole and the modelled impedances of the upstream and downstream domains. It is shown that the knowledge of this global impedance along the real ω -axis provides an instability criterion and a prediction of the eigenvalues of the full system. Validations against the solutions of the eigenvalue problem obtained from the linearized fully compressible formulation confirm the accuracy of the approach. Then, it is subsequently used to characterise the range of existence of instabilities as a function of the Reynolds number, the Mach number, the aspect ratio of the hole and (for the cavity configuration) the dimensionless volume of the cavity.

Key words: jet noise, shear-flow instability

1. Introduction

Plates with orifices are very common elements adopted in numerous industrial applications, like, for example, silencers, fuel injectors or wind instruments.

† Email address for correspondence: fgiannetti@unisa.it

Under the effect of a harmonic incident acoustic wave, the vortex sheet formed at the lip of the aperture becomes periodically modulated and acts as an amplifier due to a Kelvin–Helmholtz instability, reorganising the jet into an arrangement of vortex rings. The generation of vorticity is an efficient mechanism to dissipate acoustic energy, as a consequence, the use of multiple perforated plates traversed by a mean flow is widely employed as a sound attenuator device for industrial applications, such as gas turbine combustion systems. These systems may suffer from thermoacoustic instabilities because of the potential for unsteady heat release, which can damage the combustion system itself. The flow through a perforated liner with bias flow has been studied experimentally by Heuwinkel, Enghardt & Rohle (2007) while Hughes & Dowling (1990), Eldredge & Dowling (2003) and Rupp, Carrotte & Macquisten (2012) have conducted both experimental and theoretical investigations. There are, however, situations where the flow through a hole can lead to the opposite effect, namely spontaneous self-oscillations and sound emissions. A particularly favourable situation with respect to sound emission is the flow through two successive holes, as encountered, for instance, in bird calls and tea kettle whistles (Henrywood & Agarwal 2013; Longobardi *et al.* 2021). Although less common, the flow through a single hole can also lead to powerful sound emissions. As in other related examples of aeroacoustic resonators, (including, for instance, the ‘edge tone’ encountered in the mouthpiece of a recorder or organ pipe), two situations may occur. In the first one, the frequency of the whistling may be directly selected by that of an acoustic resonator located in the vicinity of the hole. This is, for instance, the case for the so-called ‘pipe tone’ (or pfeifenton), corresponding to a long cylindrical pipe terminated by an aperture of smaller section. In this configuration, which was intensively investigated experimentally by Anderson (1954), the frequency of the whistling directly corresponds to one of the resonance frequencies of the pipe. In the second one, the frequency may be selected by the flow itself regardless of the existence of any acoustic resonator. This situation was noted by Bouasse (1929), who observed that the flow through a hole in a thick plate separating two large chambers leads to a whistling with a frequency proportional to the thickness of the hole. This observation was rediscovered by Jing & Sun (2000) and Su *et al.* (2015) who, in an effort to improve the performance of perforated plates as sound dampers, reported that, in some circumstances, these devices could lead to self-sustained whistling. In music acoustics one observes the interaction between the two type of mechanisms, cf. Coltman (1976). In the case of the flue instrument, the so-called edge-tone oscillation can coexist with the pipe tone and under some specific circumstances, as, for example, during the attack transients, it may be dominant, cf. Castellengo (1999). Verge, Hirschberg & Causse (1997) proposed a lumped model for flue instruments where these two feedback loops can coexist and interfere: a hydrodynamic loop responsible for the edge tone and a cavity loop responsible for the pipe tone. On the contrary, in the case of the flow past an aperture both mechanisms are associated with the same feedback loop, which is modified by placing a cavity upstream of the perforation. These two situations respectively correspond to the so-called class III and class II categories of aeroacoustic resonators, following the classification of Chanaud (1970).

Recently, Fabre *et al.* (2019) used the linearized Navier–Stokes equations (LNSE) approach to investigate the unsteady flow through a circular aperture in a thin plate subjected to harmonic forcing. A novel non-reflecting boundary condition called the complex mapping method (Sierra, Fabre & Citro 2020) was introduced to overcome the numerical difficulties created by the strong spatial amplification of the fluctuations. The approach allows computing in a rigorous way the impedance of the hole, namely the ratio between unsteady pressure difference across the orifice and unsteady volume

flow rate through the orifice, a quantity which can be directly introduced in more elaborate acoustical models. In that study, the authors confirmed that the LNSE can be effectively adopted to predict the impedance even in cases where the spatial evolution of the perturbations is rapidly dominated by nonlinear effects. The same approach was subsequently used by Fabre *et al.* (2020) for the case of a hole through a thick plate. An important result is that, for sufficiently thick holes, the impedance can acquire a negative real part in some ranges of forcing frequencies, indicating that energy can be extracted from the flow, thus providing a source for self-oscillations. Investigation of the structural sensitivity also allowed the authors to demonstrate that the hydrodynamic instability of the shear layer separating the jet from the recirculation bubble is the driving motor for the observed phenomenon. This corresponds to the same instability as in the jet of a flue instrument or the shear layer for a grazing flow along a cavity, cf. Dai & Aurégan (2016, 2018). In this flow configuration, the sharpness of the aperture corner creates a recirculation bubble that enhances the instability mechanism.

The response of a system to a harmonic forcing is naturally studied via a transfer function: here it corresponds to the concept of impedance, which can also be used to obtain important information regarding the stability properties of a system. First, plotting the impedance in the form of Nyquist diagrams (namely a parametric representation of $Z(\omega)$ in the complex plane for real values of ω) provides a direct way to determine the number of unstable modes of the system, as a function of the number of times the Nyquist contour encircles the origin. Secondly, when the system has a complex eigenvalue located close to the real ω -axis, an approximation of the eigenvalue can be obtained from a Taylor expansion of the impedance function around the real axis. Such methods are widely used in several fields such as in automatics or electronics, but remain underemployed in the flow instability community where eigenvalue computation remains the preferred approach. Note, however, that the second idea was recently applied successfully by Ferreira Sabino *et al.* (2020) for the problem of vortex-induced vibrations for a spring-mounted cylinder.

The links between impedance and stability properties were explored by Fabre *et al.* (2020) for the jet flow through a hole. The discussion revealed the existence of two different instability mechanisms leading to sound production: a purely hydrodynamic instability characterised by spontaneous self-oscillations existing in the absence of any incoming acoustic wave, and a conditional instability due to an over-reflection of acoustic waves. Simple criteria formulated in terms of the impedance were given for both kinds of instabilities, allowing us to determine their range of existences as a function of the hole aspect ratio and the Reynolds number. Among the studies considering a multiply perforated plate, Jing & Sun (2000) and Su *et al.* (2015) measured experimentally the impedances for several configurations with variable hole thickness parameter values, which are in good accordance with the first branch of conditional unstable modes, cf. Fabre *et al.* (2020, § 8). Moussou *et al.* (2007) studied experimentally a long pipe with a constriction for a number of values of the constriction ratio and the thickness ratio. In this study, they identified both the first and second branch of conditionally unstable modes.

In the approach of Fabre *et al.* (2020), the flow was assumed as locally incompressible, a hypothesis which is expected to be valid for small values of the square of the Helmholtz number ($He^2 = \omega^2 M^2$), and which does not directly allow predicting the acoustic field. Nevertheless, they suggested that the locally incompressible solution could be matched to outer solutions incorporating compressibility effects, leading to more elaborate models applicable in situations incorporating, for instance, acoustic resonators and radiation in an open domain.

The object of the present paper is precisely to show how the impedance computations of Fabre *et al.* (2020) based on a locally incompressible solution can be used to build a model applicable for a realistic situation involving compressibility. In addition, acoustic pressure fields, obtained from full compressible LNSE computations complement the study. Two generic situations are considered. In the first situation referred to as cavity/open configuration, the domain located upstream of the hole is considered as a closed cavity of finite volume, while the downstream domain is considered as open. We then show that the presence of the upstream resonator can effectively lead to instabilities, as predicted by the conditional instability criterion. The second situation, referred to as open/open configuration, corresponds to the case where the two regions, upstream and downstream of the hole, are considered as open domains of large dimension. We show, in this case, that an instability of purely a hydrodynamic type can arise.

The paper is organized as follows. In § 2 the two generic situations are introduced, and the parameters are outlined. In § 3 we introduce an asymptotically matched or lumped model which allows defining a global impedance for the selected configuration by combining the hole impedance as computed by Fabre *et al.* (2020) and the impedances of the upstream and downstream domains. We also show that a Taylor expansion of this impedance around the real ω -axis can be used to obtain an instability criterion and an estimation of the eigenvalue of the unstable modes in the fully compressible case. In § 4 we introduce a numerical resolution method for the eigenvalue problem in a fully compressible set-up. In § 5 we present results for the cavity/open configuration. We compare both approaches, demonstrating that the asymptotic model is effectively accurate for low Mach numbers. We then provide a parametric study for both problems, thanks to the asymptotic model. Section 6 presents results for the open/open configuration. We particularly investigate the effect of compressibility on the purely hydrodynamic instability mechanism identified by Fabre *et al.* (2020), and also consider the acoustic directivity of far-field sound emission.

2. Problem definition

2.1. Fluid parameters

The fluid is considered as a perfect gas with specific constant R_g and adiabatic index $\gamma = 1.4$. We denote with ρ_0 the reference density and with T_0 the reference temperature (both corresponding to the values in the upstream domain). The fluid is assumed to have constant dynamic viscosity μ and heat conductivity α . The mass flow rate at the inlet of the domain is denoted with \dot{m}_0 , while the mean velocity across the hole is $U_M = \dot{m}_0 / (\rho_0 \pi R_h^2)$. Based on this velocity scale and the hole diameter $D_h = 2R_h$, the Reynolds and Mach numbers of the flow are then defined as

$$Re = \frac{\rho_0 D_h U_M}{\mu} \equiv \frac{2\dot{m}_0}{\pi R_h \mu}; \quad M = \frac{U_M}{c_0} \quad \text{with } c_0 = \sqrt{\gamma R_g T_0}. \quad (2.1a,b)$$

The fluid is also characterised by a Prandtl number $Pr = \rho_0 \alpha / \mu$ which is here assumed to be $Pr = 0.7$.

2.2. Open/open configuration

In the first configuration, termed open/open configuration and sketched in figure 1, we consider that a plate separates two semi-infinite ‘open domains’ of large dimensions. By ‘open domain’ we mean that acoustic waves generated at either side of the hole

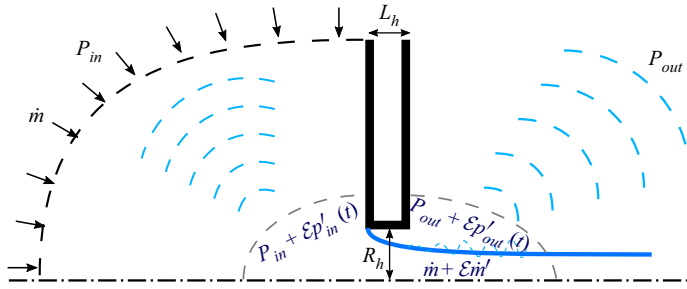


Figure 1. Sketch of the open/open configuration.

propagate towards infinity without reflection. Denoting with L_h the thickness of the plate, the geometry is thus completely defined by a single dimensionless parameter, the aspect ratio of the hole, defined as

$$\beta = \frac{L_h}{2R_h} = \frac{L_h}{D_h}. \quad (2.2)$$

In the fully compressible simulations, boundary conditions have to be applied at the boundary of the domain. For simplicity, a half-spherical boundary is considered upstream, and a uniform radial velocity is imposed, as sketched in the figure. Non-reflective boundary conditions used for the compressible computations are introduced and explained in details in § 4.

2.3. Cavity/open configuration

The second considered configuration, termed cavity/open configuration, is sketched in figure 2. This configuration is selected here to study, in the simplest possible setting, the coupling of the hole with a cavity acting as a resonator. The upper domain is considered as a cavity of dimensions L_{in}, R_{in} which acts as a Helmholtz resonator. Therefore, only its volume is relevant, not the exact dimensions L_{in}, R_{in} or the particular geometry. Thus, in addition to the aspect ratio β defined above, a second geometrical parameter enters the problem, namely the dimensionless volume defined as

$$V_{in} = \frac{L_{in} \pi R_{in}^2}{R_h^3}. \quad (2.3)$$

The inlet condition is imposed at the leftmost boundary where, for simplicity, a constant velocity profile is enforced, as sketched in the figure.

3. Matched asymptotic model

Before considering the resolution of the problem in a fully compressible setting, we detail here a matched asymptotic model which allows us to compute a total impedance characterising the behaviour of linear perturbations of the full system. We first explain how the different regions of the flow domain can be described to obtain the model, and then discuss how the derived total impedance can be used to predict the onset of instabilities.

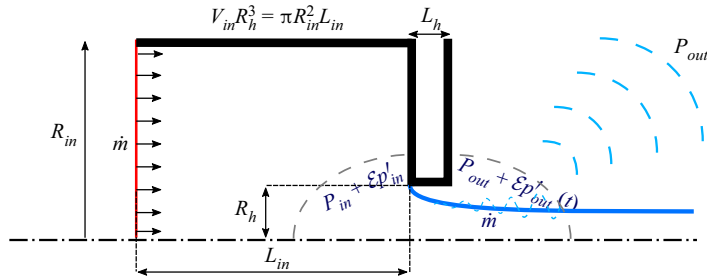


Figure 2. Sketch of the cavity/open configuration.

3.1. Matching principle

Under the hypothesis that the Mach number is small and that acoustic wavelengths are much larger than the dimensions of the hole (acoustic compactness hypothesis), it is possible to assume that the flow in the vicinity of the hole is locally incompressible, while compressibility is only relevant in the upstream and downstream domains. This hypothesis is at the origin of the asymptotically matched or lumped model. The ingredients required for matching are the pressure $p_{in}(t)$ just upstream of the hole, the pressure $p_{out}(t)$ just downstream of the hole, and the volume flow rate $q(t)$ across the hole. Working in the frequency domain, all these quantities are expanded as a constant value associated with the base flow, plus a perturbation with harmonic dependency $e^{-i\tilde{\omega}t}$, where $\tilde{\omega}$ is a (possibly complex) dimensional frequency,

$$\left. \begin{aligned} p_{in}(t) &= P_{in} + p'_{in} e^{-i\tilde{\omega}t}, & p_{out}(t) &= P_{out} + p'_{out} e^{-i\tilde{\omega}t}, \\ q(t) &= Q_0 + q' e^{-i\tilde{\omega}t}. \end{aligned} \right\} \quad (3.1)$$

It is important to understand that here p'_{out} corresponds to the level of the fluctuating pressure field at distances $\|x\|$ considered large in relation to the hole dimension but small compared with the acoustic wavelength, i.e. $R_h \ll \|x\| \ll \tilde{\lambda}$, with $\tilde{\lambda} = 2\pi c_0/\tilde{\omega}$. Consequently, this pressure level corresponds both to the outer limit for the inner solution, and to the inner limit for the outer solution of the classic matched asymptotic expansion procedure. The same holds for p'_{in} which is also used as a matching limit between inner and outer solutions.

3.2. Impedance modelling

3.2.1. Inner region: hole impedance

The inner region, located in the vicinity of the hole (delimited by dotted lines in figures 1 and 2), is governed by the incompressible LNSE. A resolution method for this problem was introduced and validated in Fabre *et al.* (2020): for the benefit of the reader, this approach is also briefly summarised in § A. The cited method allows us ultimately to deduce the (dimensionless) hole impedance $Z_h(\omega)$ defined as

$$Z_h(\omega) = \left[\frac{R_h^2}{\rho_0 U_M} \right] \frac{p'_{in} - p'_{out}}{q'}. \quad (3.2)$$

Here the factor $R_h^2/(\rho_0 U_M)$ is introduced to turn the impedance into a dimensionless one, since the dimensional impedance $(p'_{in} - p'_{out})/q'$ has physical units $\text{kg s}^{-1} \text{m}^{-4}$ in the international system, and it is a function of the dimensionless frequency $\omega = R_h \tilde{\omega}/U_M$.

The impedance is ultimately searched as $Z_h = \mathbf{P} \cdot (\mathbf{LNS} + i\omega\mathbf{B})^{-1} \cdot \mathbf{F}$, where \mathbf{F} represents a forcing of the LNSE by an imposed flow rate, $(\mathbf{LNS} + i\omega\mathbf{B})^{-1}$ is the linear resolvent of the incompressible LNSE, and \mathbf{P} is an operator allowing us to extract the overall pressure jump from the linear perturbation. After a convenient discretization, computation of the impedance is thus straightforward and only requires inversion of a single linear problem. More details are given in [Appendix A](#). It is thus much faster in comparison to eigenvalue computation, which, using the shift-and-invert method, typically requires numerous iterative resolutions of such problems. Once $Z_h(\omega)$ is computed and tabulated (Fabre *et al.* 2020) a complete parametric study in terms of Mach number and the cavity volume can be performed as shown below.

3.2.2. Downstream region: radiation impedance

When observed from a large distance, the hole can be seen as a monopolar source, which classically gives rise to spherical diverging waves. This is classically described by a radiation impedance defined as the ratio between pressure p'_{out} and flow rate q' . This impedance can be obtained by asymptotically matching an acoustically compact inner solution with a monopolar acoustic source, cf. Fletcher & Rossing (2012), Pierce (2019) and Rossing (2007). The computation is also reproduced in Fabre *et al.* (2020, Appendix A therein). When expressed in dimensionless variables, the result is a purely real impedance Z_{rad} given by

$$Z_{rad} = \left[\frac{R_h^2}{\rho_0 U_M} \right] \frac{p'_{out}}{q'} = \frac{M\omega^2}{2\pi}. \quad (3.3)$$

3.2.3. Upstream region: case of an open domain

In a similar way, in the case of the ‘open domain’ ([figure 1](#)), one can introduce the impedance of the inlet domain Z_{in} , which is defined as

$$Z_{in} = \left[\frac{R_h^2}{\rho_0 U_M} \right] \frac{p'_{in}}{q'} = -\frac{M\omega^2}{2\pi} = -Z_{rad}. \quad (3.4)$$

3.2.4. Upstream region: case of a cavity

In the case where the upstream domain is considered as a closed cavity ([figure 2](#)), we assume that this cavity acts as a Helmholtz resonator, namely the pressure $p' = p'_{in}$, and the density $\rho' = \rho'_{in}$ are uniform. Then a mass budget leads to

$$V_{in} c_0^2 \frac{d\rho'_{in}}{dt} = V_{in} \frac{dp'_{in}}{dt} = \rho_0 q', \quad (3.5)$$

which allows the introduction of the impedance of the cavity Z_{cav} ,

$$Z_{cav} = \left[\frac{R_h^2}{\rho_0 U_M} \right] \frac{p'_{in}}{q'} = \frac{i}{\omega M^2 V_{in}} = \frac{i}{\omega \chi}, \quad \chi = M^2 V_{in}. \quad (3.6)$$

Note that this expression indicates that the cavity acts as a capacitor for an electrical circuit or as a spring in a mechanical system. Moreover, its characteristics only depend upon the quantity $\chi = M^2 V_{in}$ which combines the Mach number and the dimensionless volume of the cavity. Such a model could be complemented with the addition of two other terms

that have been neglected. In particular, one could include on the left-hand side of the mass balance the deviation from isentropic pressure fluctuations due to, for instance, the effects of the thermal boundary layer and on the right-hand side, the convective term involving density fluctuations. These terms have been neglected based on the fact that velocity and temperature gradients within the cavity are small as long as the ratio between the height of the cavity and the radius of the hole is large. In our study, this corresponds to $L_{in} = R_{in} = (V_{in}/\pi)^{1/3} \gg R_h$, which holds for the cavities analysed in this study.

3.2.5. Summary: total impedance of the problem

Regrouping all the regions, we are now able to obtain a single constitutive equation for the total impedance of the system, denoted either as Z_a or Z_b for the two investigated configurations, which allows us to determine the eigenfrequencies of the complete problem.

(a) For the open/open configuration, $Z_h = -2Z_{rad}$, or equivalently,

$$Z_a(\omega) = Z_h(\omega) + \frac{M\omega^2}{\pi} = 0. \quad (3.7)$$

(b) For the cavity/open configuration, $Z_h = -Z_{cav} - Z_{rad}$, or equivalently,

$$Z_b(\omega) = Z_h(\omega) + \frac{M\omega^2}{2\pi} + \frac{i}{M^2 V_{in} \omega} = 0. \quad (3.8)$$

We emphasize that the total impedance defined here is designed mainly to be used to detect eigenvalues, hence, only the condition $Z(\omega) = 0$ is significant. The complex zeros $\omega = \omega_R + i\omega_I$ of Z then correspond to the eigenmodes of the system, and the system is therefore unstable if there exists such a zero with $\omega_I > 0$. When not zero, there is no direct physical interpretation to the value $Z(\omega)$ associated with a given ω . Schematically, $1/Z$ can be conceived of as a measure of the response of the system to an imposed forcing, so that $Z = 0$ means that the response is infinite, or in other words that a solution without forcing is possible. For instance, Fabre *et al.* (2020, Appendix A therein) considered the case where the forcing corresponds to a spherically converging wave coming from downstream; in this case the reflection coefficient is effectively proportional to Z^{-1} (see equation (A12) in this reference). Other kinds of forcing could be considered, leading to the same conclusion. In the present paper we remain to an intuitive interpretation of Z^{-1} and do not elaborate on the link between the impedance and any specific forcing.

3.3. Predicting instability from a Taylor expansion of the impedance

As stated in the introduction, knowledge of the impedance function $Z(\omega)$ along the real ω -axis allows obtaining important information regarding instability properties of the system in two ways. First, Cauchy's argument principle (see Appendix C) can be used as a graphical method to determine whether or not an instability exists. This argument is developed in § C. Second, eigenvalues located close to the real axis may be expected to be accurately predicted from a Taylor expansion of the impedance around the real axis. This argument is presented here.

3.3.1. Asymptotic prediction of eigenvalue for the cavity/open configuration

Following an idea previously used in Ferreira Sabino *et al.* (2020) for the problem of vortex-induced vibrations of a spring-mounted cylinder, we assume here that the

impedance of the full system is mostly reactive. In the present case, this means that the impedance is dominated by its imaginary part, while the real parts (i.e. $\text{Re}(Z_h)$ and the radiation impedance) correspond to lower-order terms. Such a hypothesis, together with the fact that the flow is acoustically compact within the region of the hole, allow the use of an asymptotic expansion truncated at first order to determine the zeros of the impedance. We first elaborate this idea for the cavity/open configuration. The hypotheses are as follows:

- (i) $|\text{Re}(Z_h)| \ll |\text{Im}(Z_h)|$, i.e. $|\text{Re}(Z_h)| \sim \varepsilon |\text{Im}(Z_h)|$;
- (ii) $M\omega^2/2\pi \ll |\text{Im}(Z_h)|$, i.e. $M\omega^2/2\pi \sim \varepsilon |\text{Im}(Z_h)|$.

Here the real parameter $0 < \varepsilon \ll 1$. Note that hypothesis (i) is not justified for every value of ω_0 since from the results of Fabre *et al.* (2020) the real and imaginary parts of Z_h are generally of comparable order of magnitudes. However, this hypothesis can be expected to be valid in the vicinity of the threshold of the instability. Hypothesis (ii) is needed for the acoustic compactness and, therefore, directly satisfied.

Consider the frequency expansion

$$\omega = \omega_0 + \varepsilon\omega_1, \quad \omega_0 \in \mathbb{R}, \quad \omega_1 \in \mathbb{C}, \quad \varepsilon \in \mathbb{R}, \quad (3.9)$$

and let us substitute ω in (3.8) by (3.9) and by performing a Taylor expansion in terms of the assumed small quantities leads to

$$\begin{aligned} Z_b(\omega) = & i \left[\text{Im}(Z_h(\omega_0)) + \frac{1}{M^2 V_{in} \omega_0} \right] \\ & \varepsilon \left[\text{Re}(Z_h(\omega_0)) + \frac{M\omega_0^2}{2\pi} + \left(\left(\frac{\partial Z_h}{\partial \omega} \right)_{\omega=\omega_0} - \frac{i}{M^2 V_{in} \omega_0^2} \right) \omega_1 \right] \\ & + O(\varepsilon^2), \end{aligned} \quad (3.10)$$

where $O(\varepsilon^2)$ denotes higher-order terms as a function of the assumed small parameter. The condition $Z_b = 0$ then leads to the following results.

- (i) The zeroth-order terms lead to the condition

$$-\omega_0 \text{Im}(Z_h(\omega_0)) = \frac{1}{M^2 V_{in}} = \frac{1}{\chi}. \quad (3.11)$$

- (ii) The first-order term leads to

$$\begin{aligned} \text{Im}(\omega_1) = & \frac{\left[\text{Re}(Z_h(\omega_0)) + \frac{M\omega_0^2}{2\pi} \right] \left(\left(\frac{\partial \text{Im}(Z_h(\omega))}{\partial \omega_R} \right)_{\omega=\omega_0} - \frac{1}{\chi \omega_0^2} \right)}{\left(\left(\frac{\partial \text{Re}(Z_h(\omega))}{\partial \omega_R} \right)_{\omega=\omega_0} \right)^2 + \left(\left(\frac{\partial \text{Im}(Z_h(\omega))}{\partial \omega_R} \right)_{\omega=\omega_0} - \frac{1}{\chi \omega_0^2} \right)^2}, \\ \text{Re}(\omega_1) = & \frac{- \left[\text{Re}(Z_h(\omega_0)) + \frac{M\omega_0^2}{2\pi} \right] \left(\frac{\partial \text{Re}(Z_h)}{\partial \omega_R} \right)_{\omega=\omega_0}}{\left(\left(\frac{\partial \text{Re}(Z_h(\omega))}{\partial \omega_R} \right)_{\omega=\omega_0} \right)^2 + \left(\left(\frac{\partial \text{Im}(Z_h(\omega))}{\partial \omega_R} \right)_{\omega=\omega_0} - \frac{1}{\chi \omega_0^2} \right)^2} \end{aligned} \quad (3.12)$$

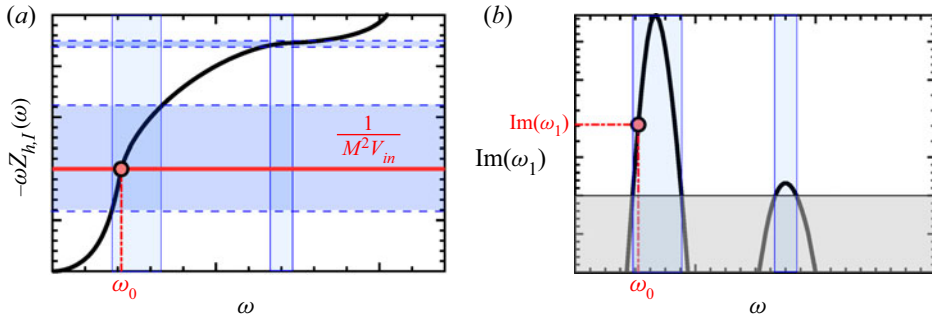


Figure 3. Linear scale representation of the zero computation of (3.9) with the (a) zeroth-order (3.11) and (b) first-order (3.12) approximations.

The imaginary part of the first-order correction directly provides a criterion of stability. Provided that the imaginary part of $\partial Z_h / \partial \omega$ is negative (a condition which is found to hold in all cases where the starting hypotheses are verified), then it is possible to conclude that an instability is possible as soon as

$$\text{Re}(Z_h(\omega_0)) < -\frac{M\omega_0^2}{2\pi}. \quad (3.13)$$

We recognize here an improved version of the conditional instability criterion of Fabre *et al.* (2020). Physically, this condition means that the energy extracted from the base flow $-\text{Re}(Z_h(\omega_0))|q'|^2/2$ must be larger than the energy radiated $Z_{rad}|q'|^2/2$.

Fabre *et al.* (2020) have documented the function $Z_h(\omega)$ for real values of ω over a wide range of parameters. Once the hole impedance function $Z_h(\omega)$ is determined, these results can be used to solve the coupled conditions (3.11), (3.12) and ultimately to obtain an instability criterion and an estimate for the growth rate. Figure 3 explains graphically these conditions. The resolution can be done in two ways. Via a direct method, that is, given the parameters M and V_{in} , one first solves for (3.11), which is an implicit equation in ω_0 as a function of the parameter χ (as sketched in figure 3a). Then one may deduce $\text{Im}(\omega_1)$ which is an explicit function of ω_0 and M (as sketched in figure 3b) and it ultimately provides a criterion of instability.

An alternative is to follow an inverse method. Given M , we first consider $\text{Im}(\omega_1)$ as a function of ω_0 and deduce the ranges of ω_0 where this function is positive (as indicated in blue on figure 3b). Once these unstable ranges are known, we deduce the corresponding ranges for $1/(M^2 V_{in})$ by using (3.11) (as indicated by blue ranges in figure 3a). The approach thus indicates the ranges of V_{in} where, for the given M , the jet is unstable. The great advantage of this inverse method is that the equation (3.11) is explicit when solving for V_{in} in terms of ω_0 .

The inverse method is a very efficient way to obtain an estimation of the eigenvalue of the full problem $\omega = \omega(\text{Re}, \beta, M, V_{in})$ provided one disposes of a tabulation of the function $Z_h(\omega; \text{Re}, \beta)$ for real values of ω . It must be emphasised that the number of parameters has been reduced from four to only two, as V_{in} and M only occur through the modelled impedance of the upstream and downstream domains. However, the reduction relies on a series of strong hypotheses: first $M \ll 1$ and $|\omega| \ll 1/M$ for the matched asymptotic model to hold, and second the assumptions used to treat $\text{Re}(Z_h)$ as a correction. The validity of the approach, therefore, has to be assessed by comparing the results with

those obtained using a fully compressible model in order to clarify the range of validity of the used approximations, as detailed in § 5.1.

3.3.2. Asymptotic prediction of eigenvalue for the open/open configuration

Let us now follow a similar route to achieve an estimation of the eigenvalue ω for the open/open configuration. In this case, the zeroth-order and first-order corrections simplify to

$$-\omega_0 \text{Im}(Z_h)(\omega_0) = 0, \quad (3.14)$$

$$\left. \begin{aligned} \text{Im}(\omega_1) &= \frac{\left[\text{Re}(Z_h(\omega_0)) + \frac{M\omega_0^2}{\pi} \right] \left(\frac{\partial \text{Im}(Z_h)}{\partial \omega_R} \right)_{\omega=\omega_0}}{\left| \left(\frac{\partial Z_h}{\partial \omega} \right)_{\omega=\omega_0} \right|^2}, \\ \text{Re}(\omega_1) &= \frac{- \left[\text{Re}(Z_h(\omega_0)) + \frac{M\omega_0^2}{\pi} \right] \left(\frac{\partial \text{Re}(Z_h)}{\partial \omega_R} \right)_{\omega=\omega_0}}{\left| \left(\frac{\partial Z_h}{\partial \omega} \right)_{\omega=\omega_0} \right|^2}, \end{aligned} \right\} \quad (3.15)$$

where the non-zero ω_0 are the zeros of the imaginary part of the hole impedance function $\text{Im}(Z_h)$ and the growth rate is estimated by (3.15).

Note that this expression is identical to the one obtained for the cavity/open configuration when $V_{in} \rightarrow \infty$, except for the radiation term, which is twice the value in the previous case. This accounts for the fact that radiation occurs on both sides, so that total radiation losses are twice larger.

4. Full compressible formulation

After detailing the matched asymptotic model, we now introduce in this section a numerical method to resolve directly the eigenvalue problem in a fully compressible setting.

4.1. Compressible Navier–Stokes equations

Let us consider a compressible fluid motion of a perfect gas described in primitive variables by $\mathbf{q} = [\rho, \mathbf{u}, T, p]^T$, where the velocity vector field is $\mathbf{u} = (u, v, w)$, pressure p , temperature T and fluid density ρ . Dimensional primitive variables have been made dimensionless, as follows:

$$\mathbf{x} = \frac{\mathbf{x}}{D_h}, \quad t = \frac{\tilde{t} U_M}{D_h}, \quad \rho = \frac{\tilde{\rho}}{\rho_{ref}}, \quad \mathbf{u} = \frac{\tilde{\mathbf{u}}}{U_M}, \quad T = \frac{\tilde{T}}{T_{ref}}, \quad p = \frac{\tilde{p} - p_{ref}}{\rho_{ref} U_M^2}. \quad (4.1a-f)$$

Here dimensional values are designated by an upper tilde $\tilde{\cdot}$, and reference values are indicated with the \cdot_{ref} . Dynamics is governed by the compressible Navier–Stokes equations, which are here written in terms of primitive dimensionless variables in the

compact vector notation

$$\mathbf{M} \left(\frac{\partial \mathbf{q}}{\partial t} \right) = \mathcal{NS}(\mathbf{q}) = \mathbf{L}(\mathbf{q}) + \mathbf{N}(\mathbf{q}) + \mathbf{C} = \mathbf{0}, \quad (4.2)$$

where $\mathbf{C} = [0, \mathbf{0}, 0, 1]^T$, the mass matrix \mathbf{M} and the linear operator \mathbf{L} are defined as

$$\mathbf{M} = \begin{pmatrix} 1 & 0 & 0 & 0 \\ 0 & \rho \mathbf{I} & 0 & 0 \\ 0 & 0 & \rho & 0 \\ 0 & 0 & 0 & 0 \end{pmatrix}, \quad \mathbf{L} = \begin{pmatrix} 0 & 0 & 0 & 0 \\ 0 & -\nabla \cdot \boldsymbol{\tau}(\cdot) & 0 & \nabla \\ 0 & 0 & -\frac{\gamma}{Pr Re} \Delta & 0 \\ 0 & 0 & 0 & \gamma M^2 \end{pmatrix}, \quad (4.3a,b)$$

while the nonlinear operator is written as

$$\mathbf{N}(\mathbf{q}) = \begin{pmatrix} \mathbf{u} \cdot \nabla \rho + \rho \nabla \cdot \mathbf{u} \\ \rho \mathbf{u} \cdot \nabla \mathbf{u} \\ (\gamma - 1) [\rho T \nabla \cdot \mathbf{u} - \gamma M^2 \boldsymbol{\tau}(\mathbf{u}) : \mathbf{D}(\mathbf{u})] + \rho \mathbf{u} \cdot \nabla T \\ -\rho T \end{pmatrix}. \quad (4.4)$$

Here $\mathbf{D} = 1/2(\nabla \mathbf{u} + \nabla \mathbf{u}^T)$ is the rate of strain tensor and $\boldsymbol{\tau}$ is the viscous stress tensor defined as $\boldsymbol{\tau} = 2\mu \mathbf{D} - 2\mu/3 \nabla \cdot \mathbf{u} \mathbf{I}$.

4.2. Compressible Navier–Stokes – base flow equations

The stability of a steady-state solution to infinitesimal perturbations can be analysed using the classical approach based on linearization of the governing equations: the total flow field is expanded into the sum of a steady-state term plus an infinitesimally small unsteady harmonic perturbation as

$$\mathbf{q}(t) = \mathbf{q}_0 + \varepsilon \left(\hat{\mathbf{q}} e^{-i\omega t} + \text{c.c.} \right), \quad (4.5)$$

where $\varepsilon \ll 1$. Inserting (4.5) in the governing equations (4.2) and neglecting quadratic terms leads to two problems, one for the base flow and one for the perturbation. In particular, at leading order, only steady terms are kept, which leads to the steady Navier–Stokes equations

$$\mathcal{NS}(\mathbf{q}_0) = \mathbf{L}(\mathbf{q}_0) + \mathbf{N}(\mathbf{q}_0) + \mathbf{C} = \mathbf{0}, \quad (4.6)$$

complemented with appropriate boundary conditions. No-slip adiabatic boundary conditions are used at the walls (4.7c). At the axis of revolution, the radial component v_0 is set equal to zero, and the radial derivative of the remaining terms is null (4.7d). At the outlet we set stress-free and isothermal boundary conditions (4.7b); in this way the pressure at the outlet is equal to the thermodynamic pressure, i.e. $p_0 = 1$. Finally, at the inlet boundary $\Gamma_{in} = \Gamma_{in,0} \cup \Gamma_{in,1}$, a constant mass flow is enforced on the $\Gamma_{in,0}$ boundary, slip condition, constant density and zero thermal flux are imposed on the $\Gamma_{in,1}$ (4.7a). Summarising,

$$\rho_0|_{\Gamma_{in}} = 1, \quad \int_{\Gamma_{in,0}} \rho_0 \mathbf{u}_0 \cdot \mathbf{n} \, dS = \frac{\pi}{4}, \quad (\mathbf{u}_0 \cdot \mathbf{n})|_{\Gamma_{in,1}} = 0, \quad (\nabla T_0 \cdot \mathbf{n})|_{\Gamma_{in}} = 0, \quad (4.7a)$$

$$T_0|_{\Gamma_{out}} = 1, \quad (-p_0 \mathbf{I} + \boldsymbol{\tau}(\mathbf{u}_0)) \cdot \mathbf{n}|_{\Gamma_{out}} = 0, \quad (4.7b)$$

$$\mathbf{u}_0|_{\Gamma_w} = (0, 0, 0)^T, \quad (\nabla T_0 \cdot \mathbf{n})|_{\Gamma_w} = 0, \quad (4.7c)$$

$$v_0|_{\Gamma_w} = 0, \quad \frac{\partial u_0}{\partial r} = \frac{\partial w_0}{\partial r} = \frac{\partial \rho_0}{\partial r} = \frac{\partial T_0}{\partial r} = \frac{\partial p_0}{\partial r} = 0 \quad \text{on } \Gamma_{axis}. \quad (4.7d)$$

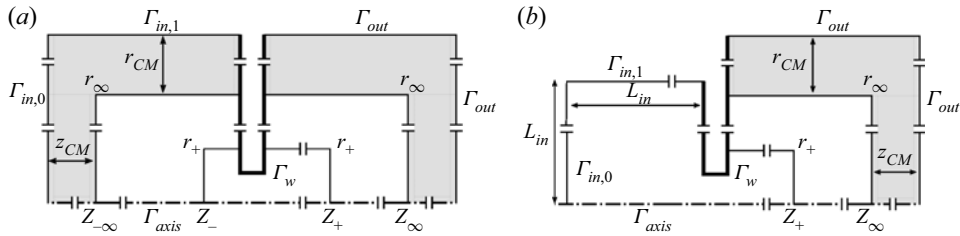


Figure 4. Schematic representation of the computational mesh for both configurations, (a) open/open case, (b) closed/open case: $z_{-\infty}$, z_{∞} , r_{∞} are, respectively, the location of the physical inlet, outlet and lateral boundaries. The physical domain is padded into a complex mapping layer with a radial extension r_{CM} (respectively axial z_{CM} extension). The inner domain corresponds to an inner region with the highest vertex density: z_{-} , z_{+} , r_{+} are, respectively, the location of the left, right and lateral boundaries of this inner domain; in the closed/open case the inner domain includes the cavity located upstream of the hole.

4.3. Linearized compressible Navier–Stokes equations – homogeneous problem

The linearized compressible Navier–Stokes equations govern the evolution of the perturbation \hat{q} ,

$$-i\omega \mathbf{M}\hat{q} = \mathbf{LNS}_0(\hat{q}) = [\mathbf{L} + DN|_{q_0}]\hat{q}, \quad (4.8)$$

where $DN|_{q_0}$ is the Jacobian matrix of the nonlinear operator evaluated at the steady state q_0 .

With the purpose of modelling a large container upstream of the hole, for the open/open case, we have designed a computational domain, [figure 4\(a\)](#), composed of three regions: an inner domain with the highest vertex density, the physical domain and an absorbing layer to eliminate the appearance of spurious eigenvalues. The absorbing layer corresponds to the complex mapping technique, cf. [Sierra et al. \(2020\)](#). The boundary conditions of the linearized full compressible formulation for the open/open case are as follows:

$$\hat{\rho}|_{\Gamma_{in}} = 0, \quad (-\hat{p}\mathbf{I} + \tau(\hat{\mathbf{u}})) \cdot \mathbf{n}_{\Gamma_{out}} = 0, \quad (\nabla \hat{T} \cdot \mathbf{n})|_{\Gamma_{in}} = 0, \quad (4.9a)$$

$$\hat{\rho}|_{\Gamma_{out}} = 0, \quad (-\hat{p}\mathbf{I} + \tau(\hat{\mathbf{u}})) \cdot \mathbf{n}_{\Gamma_{out}} = 0, \quad (\nabla \hat{T} \cdot \mathbf{n})|_{\Gamma_{out}} = 0, \quad (4.9b)$$

$$\hat{\mathbf{u}}|_{\Gamma_w} = (0, 0, 0)^T, \quad (\nabla \hat{T} \cdot \mathbf{n})|_{\Gamma_w} = 0, \quad (4.9c)$$

$$\hat{v}|_{\Gamma_w} = 0, \quad \frac{\partial \hat{u}}{\partial r} = \frac{\partial \hat{w}}{\partial r} = \frac{\partial \hat{\rho}}{\partial r} = \frac{\partial \hat{T}}{\partial r} = \frac{\partial \hat{p}}{\partial r} = 0 \quad \text{on } \Gamma_{axis}. \quad (4.9d)$$

In particular, in the far field (inlet and outlet) we impose null density variations, a stress-free boundary condition and vanishing thermal flux ([4.9a](#)) and ([4.9b](#)); doing so the mass flux, $\rho_0 \hat{\mathbf{u}} \cdot \mathbf{n}$, is allowed to vary. A no-slip adiabatic boundary condition is used at the walls ([4.9c](#)), while at the axis the radial component of the velocity \hat{v} is set to zero, together with a null radial derivative of the remaining terms ([4.9d](#)).

For the purpose of modelling a closed cavity that acts as an acoustic resonator, we have a computational domain, which is sketched in [figure 4\(b\)](#), where the complex mapping layer is only present in the region placed downstream of the hole. The set of boundary

conditions are as follows:

$$\hat{\rho}|_{\Gamma_{in}} = 0, \quad \hat{\mathbf{u}}|_{\Gamma_{in}} = (0, 0, 0)^T, \quad (\nabla \hat{T} \cdot \mathbf{n})|_{\Gamma_{in}} = 0, \quad (4.10a)$$

$$\hat{\rho}|_{\Gamma_{out}} = 0, \quad (-\hat{p}\mathbf{I} + \tau(\hat{\mathbf{u}})) \cdot \mathbf{n}_{\Gamma_{out}} = 0, \quad (\nabla \hat{T} \cdot \mathbf{n})|_{\Gamma_{out}} = 0, \quad (4.10b)$$

$$\hat{\mathbf{u}}|_{\Gamma_w} = (0, 0, 0)^T, \quad (\nabla \hat{T} \cdot \mathbf{n})|_{\Gamma_w} = 0, \quad (4.10c)$$

$$\hat{v}|_{\Gamma_w} = 0, \quad \frac{\partial \hat{u}}{\partial r} = \frac{\partial \hat{w}}{\partial r} = \frac{\partial \hat{\rho}}{\partial r} = \frac{\partial \hat{T}}{\partial r} = \frac{\partial \hat{p}}{\partial r} = 0 \quad \text{on } \Gamma_{axis}. \quad (4.10d)$$

i.e. null density and velocity variations (4.10a) at the inlet, a stress-free condition, null density variation and vanishing thermal flux (4.10b) at the outlet; no-slip and adiabatic walls (4.10c); null radial velocity component and null radial derivative of the remaining terms (4.10d).

4.4. Numerical implementation

Following a usual route in global stability analysis, the nonlinear problem (4.6) for the base flow is solved using a Newton iteration method and the eigenvalue problem (4.8) is solved using a shift-invert Arnoldi method. Spatial discretization is done using a finite-element method, using P2-elements for velocity components u_x , u_r and P1-elements for thermodynamic variables P , ρ , T . Mesh generation and assembly of matrix operators is performed using the FreeFem++ software (Hecht 2012). Resolution is achieved using PETSc/SLEPc libraries, which are directly implemented in FreeFem++. Monitoring of computation, loop over the parameters and post-processing are handled in Matlab thanks to the StabFem suite (Fabre *et al.* 2018). Note that during the process, mesh adaptation is used in a way similar to as described in Fabre *et al.* (2018), to ensure that the resolution is sufficient to ensure grid independence when computing the base flow and the eigenmodes. Examples of codes reproducing sample results are shared on the website of the StabFem project. Some details about the computed base flows are given in Appendix B. Details about grid convergence are given in Appendix E.

5. Results – cavity/open configuration

5.1. Validation of the asymptotic model – comparison with compressible LNSE

In § 3.3.1 we introduced an asymptotic method which is able to predict the eigenvalues $\omega = \omega(Re, \beta, M, V_{in})$ from a simple tabulation/computation of the function $Z_h(\omega; Re, \beta)$ for real values of ω , hence reducing the number of parameters from four to two only. Before conducting a full parametric study of the instability with the proposed matched asymptotic method, we have to assess its validity by comparing the predictions with resolution of the full eigenvalue problem. This is done in figure 5 which compares the amplification rates (a, c, e, g) and frequencies (b, d, f, h) obtained with the two approaches for values of M , Re and V_{in} spanning a large range of parameter values, considering a hole with aspect ratio $\beta = 0.3$.

Consider, first, the predictions of the asymptotic model represented by coloured lines in the figures. Thanks to the inverse method explained in § 3.3.1, the asymptotic prediction allows us to plot ω as a continuous function of V_{in} . We use solid lines for the segments of the curves corresponding to unstable modes and dotted lines for those corresponding to stable modes. As identified by Fabre *et al.* (2020), for $\beta = 0.3$, several modes of

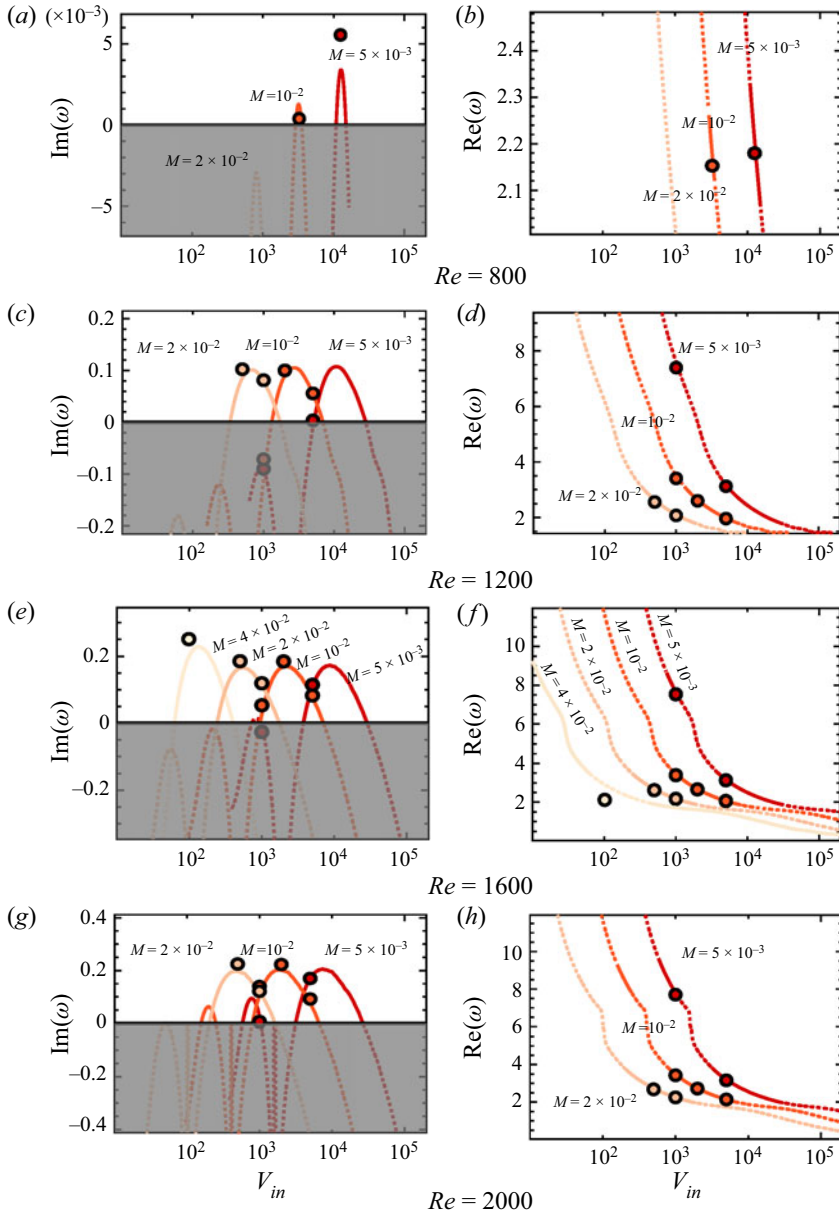


Figure 5. Growth rate (a,c,e,g) and frequency (b,d,f,h) of eigenmodes as a function of V_{in} , M and Re for $\beta = 0.3$. Lines were obtained from the matched asymptotic model and points with the compressible LNSE. Solid lines denote unstable regions, dashed lines are used for stable zones.

conditional instability, termed C_1 , C_2 , etc. . . are expected to arise as the Reynolds number is increased. The corresponding frequencies are quantized, and an argument to explain this quantification was proposed in terms of the dynamics of the shear layer. An alternative argument, in terms of a forward shear wave and a backward acoustic wave, is proposed in [Appendix D](#).

From the results of Fabre *et al.* (2020), for $\beta = 0.3$ (see also [figure 18](#) reproduced in [Appendix D](#)), the first mode C_1 arises just below $Re = 800$ and the second mode C_2 arises

for $Re \approx 1500$. This is in good agreement with the observed results of the asymptotic model, which effectively predicts two ranges of instability for $Re = 1600$ and $Re = 2000$, at least, for the smallest considered values of M . The figure also shows that increasing M results in a shifting of the instability ranges towards smaller values of V_{in} .

Consider now, the eigenvalue calculations, represented by circles in the figures. Results have been computed for a limited set of values of V_{in} where unstable modes were expected. Recall that in the eigenvalue study, V_{in} is linked to the size of the numerical domain, so that the whole process (mesh generation, base flow computation, resolution of eigenvalue problem) has to be restarted for each new value of V_{in} . An excellent matching between the two estimates may be appreciated even for large growth rates, the relative error being less than 3 % in most cases. Comparison seems poorer, at first sight, for the case of $Re = 800$ reported in [figure 5\(a\)](#) but it must be remembered that the case is very close to the threshold and amplification rates are very small, so that the absolute error is actually of comparable order to the other cases. Not that an excellent agreement is still found in cases where the amplification rate is not small, a range where the impedance criterion should be *a priori* slightly less reliable due to its perturbative nature. The agreement also remains excellent when the Mach number is raised to $M = 2 \times 10^{-2}$. Note that, for eigenvalue computations, it has been only considered configurations with $V_{in} > 10^2$, since for smaller values, the cavity becomes very small and the modelling as a Helmholtz resonator becomes questionable. This is why we did not attempt to draw any comparisons for $M > 2 \times 10^{-2}$, with the exception of a case with $M = 4 \times 10^{-2}$ represented in plot (e).

5.2. Structure of some eigenmodes

Let us now illustrate the structure of a few eigenmodes computed with the full compressible LNSE. [Figure 6](#) displays the eigenmode computed for $M = 5 \times 10^{-3}$ and $V_{in} = 10^4$ for $Re = 1200$. This mode is correctly predicted by the asymptotic model, and recognized to correspond to the branch C_1 of conditional instability modes, as defined by [Fabre *et al.* \(2020\)](#). As observed, the pressure level inside the cavity is uniform, confirming that the cavity effectively acts as a Helmholtz resonator for this mode so that the modelling hypotheses are correctly verified. Downstream of the hole, the mode is characterised by an alternance of structures of opposite sign, localized along the shear layer. This structure is characteristic of regions associated with a negative real part of impedance, as identified by [Fabre *et al.* \(2020\)](#). Note that very far away in the downstream domain, the structure is expected to match with a spherical diverging wave of the dimensionless wavelength $\lambda = 2\pi/(M\omega_R)$. Here λ is of order 70, so this structure is not visible on the figure. A characterisation of the far-field acoustic radiation is described in § 6.3; see [figure 13](#).

In addition to eigenmodes of the kind presented in [figure 6](#) which are well predicted by our asymptotic approach, one typically observes the existence of other families of eigenmodes with a more complex structure. [Figure 7\(b\)](#) displays a family of such modes, computed for the set of parameters $M = 2 \times 10^{-1}$, $V_{in} = 10^4$ for $Re = 1200$. One clearly observes that the pressure inside the cavity is no longer uniform, but characterised by nodal lines in the radial and axial distributions. These modes are recognised as cavity modes. They arise as soon as the acoustic compactness hypothesis fails, i.e. when the acoustic wavelength is smaller than the characteristic length ($L_{in} = (V_{in}/\pi)^{1/3}$) of the cavity.

5.3. Parametric study

In our previous work, the ranges of parameters corresponding to a conditional instability (requiring the presence of a correctly tuned resonator) were mapped in the Re – β plane;

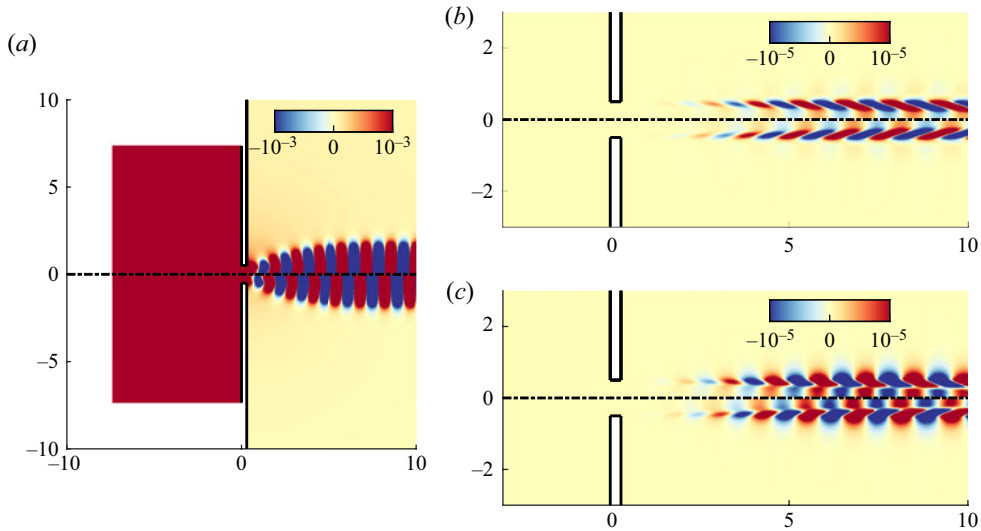


Figure 6. Plot of the C_1 eigenmode for $Re = 1200$ (real part in upper region and imaginary part in the lower region) at $M = 5 \times 10^{-3}$. (a) Pressure, (b) temperature and (c) density.

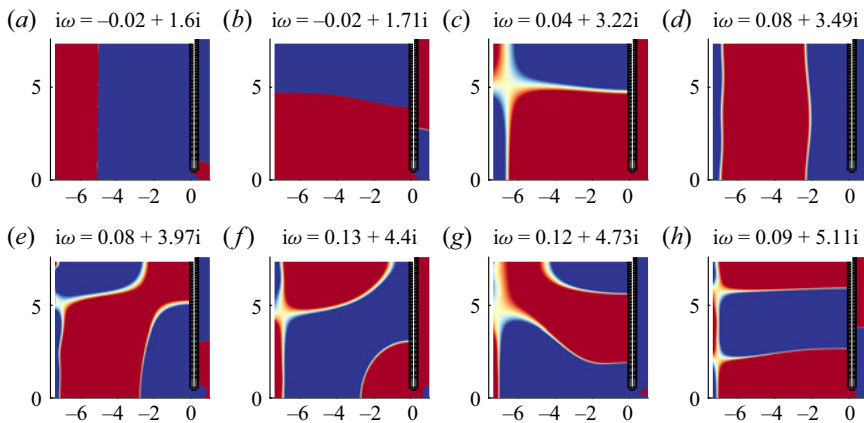


Figure 7. Real part of the pressure component of higher-order cavity modes for $M = 2 \times 10^{-1}$ and a cavity of $V_{in} = 10^4$.

see Fabre *et al.* (2020, figure 13), also reproduced in [Appendix D](#) (see figure 18). We are now able to build upon these results a parametric study of the situation where the resonator corresponds to the upstream cavity, as a function of the four parameters (Re , β , M , V_{in}). [Figures 8](#) and [9](#) display the dependence of the neutral curves on the Mach number and V_{in} for several Reynolds numbers and values $\beta = 0.3$ and $\beta = 1$, respectively. Let us first explore the value $\beta = 0.3$ displayed in [figure 8](#); there exist only two unstable modes, C_1 and C_2 . The cavity is correctly tuned to trigger the instability inside each of the bounded coloured regions of the (V_{in}, M) plane. For the configuration corresponding to $\beta = 1$, there exist four modes of conditional instability. As reported in Fabre *et al.* (2020), C_1 and C_4 instabilities only exist if the cavity connected upstream of the aperture is correctly tuned, that occurs inside each of the bounded coloured regions of the (V_{in}, M) plane of

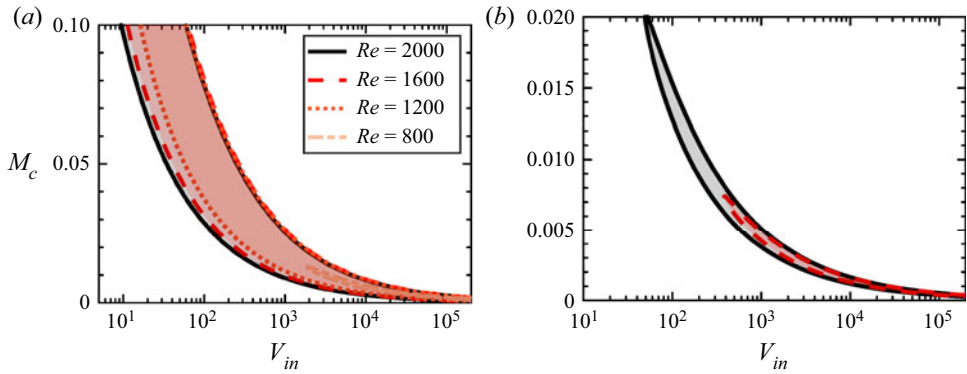


Figure 8. Regions of conditional stability in the (V_{in}, M) plane for $\beta = 0.3$; (a) C_1 , (b) C_2 .

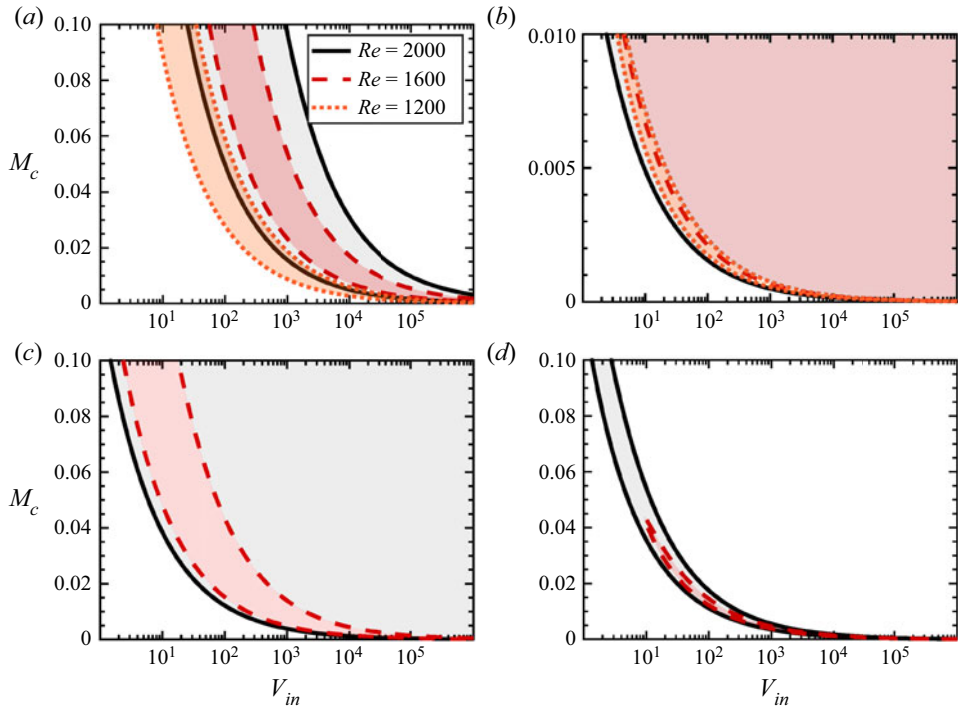


Figure 9. Regions of conditional stability in the (V_{in}, M) plane for $\beta = 1$; (a) C_1 , (b) C_2 , (c) C_3 , (d) C_4 .

figure 9(a,d). These regions of instability grow with the Reynolds number, and they shrink with V_{in} . Contrary to instabilities C_1 and C_4 , for a given value of V_{in} , instabilities C_2 and C_3 may exist for every M ; for this reason, these instabilities may be conceived as a degenerate situation of pure hydrodynamic instabilities H_2 and H_3 , which are discussed in § 6.

Finally, the dependence of this type of instability on the acoustic resonator is better appreciated if we consider the effect of V_{in} and M together with the $\chi = V_{in}M^2$ parameter. This allows us to display neutral curves of stability in the (χ, Re) plane, which is shown in figure 10 for several values of β and M , where the explicit dependence on the Mach

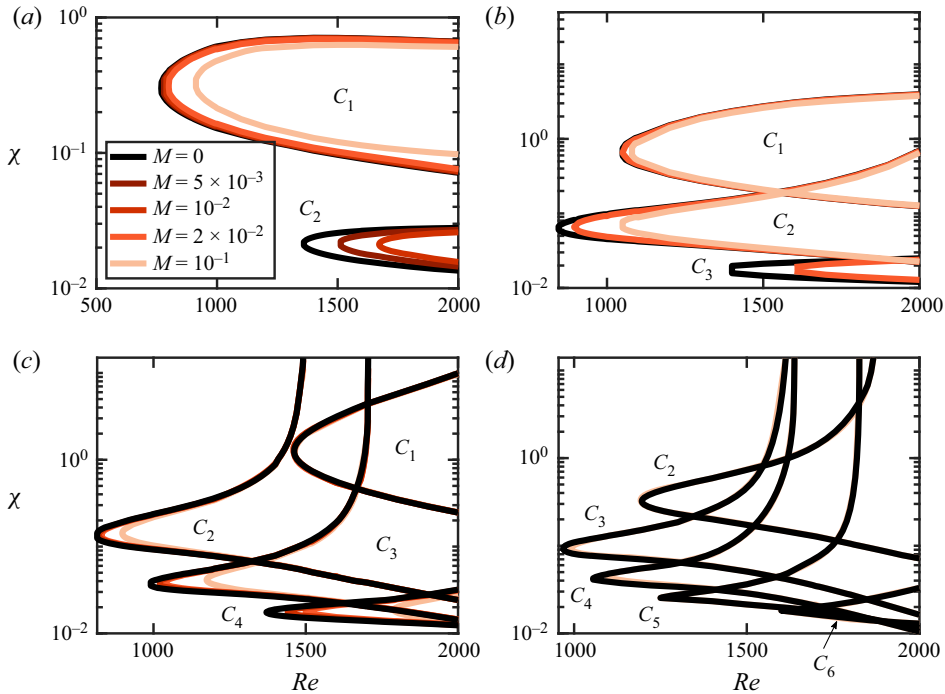


Figure 10. Regions of conditional instability in the (χ, Re) plane; (a) $\beta = 0.3$, (b) $\beta = 0.6$, (c) $\beta = 1$, (d) $\beta = 2$.

number originates from the radiation term of (3.8). Each bounded region corresponds to a conditional instability C_i ; neutral curves display the shape of a ‘tongue’ with the tip located at the lowest Reynolds number of the instability region and a vertical asymptote located at the Reynolds number of the threshold of the H_i instability (if it exists). From figure 10 we can appreciate how C_i conditional instabilities are a generalization of the pure hydrodynamic instabilities H_i . Nevertheless, a connection between hydrodynamic and conditional instabilities for limit values of χ is outside the range of validity of the methodology used for the closed/open case. In fact, one may relate the characteristic cavity length (L_{in}) and the acoustic wavelength (λ_{ac}) in terms of the Strouhal number and the parameter χ ,

$$\left(\frac{L_{in}^{3/2}}{\lambda_{ac}}\right)^2 = St^2 \frac{\chi}{\pi}, \quad (5.1)$$

which implies that, for cavities characterised by $\chi \gg 1$, one cannot rule out the existence of higher cavity modes. Such a finding is only relevant for regions near the vertical asymptotes of figure 9. The methodology remains valid for the C_1 mode, where the product $St^2(\chi/\pi) < 1$, even in the region of $\chi > 1$ for $\beta = 1$, because the Strouhal number of the C_1 mode is approximately one-fourth, cf. Appendix D.

6. Results – open/open configuration

6.1. Parametric study

A purely hydrodynamic instability exists in the present configuration for sufficiently large values of the hole aspect ratios β . In this section we check that such instabilities are

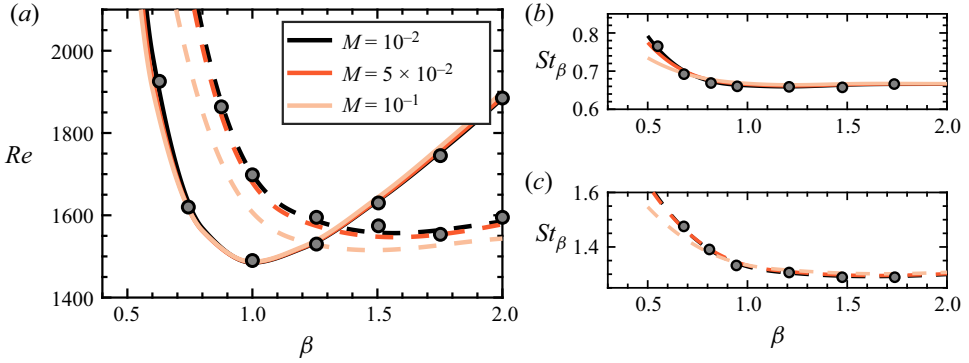


Figure 11. (a) Neutral curves of instability of hydrodynamic modes H_2 (solid lines) and H_3 (dashed lines) for $M = 10^{-2}$, 5×10^{-2} and $M = 10^{-1}$. (b) Strouhal evolution of the H_2 modes with β at the threshold of the instability. (c) The same as (b) for the H_3 modes. Dots correspond to incompressible results of Fabre *et al.* (2020), also reported in [Appendix D](#).

effectively encountered in the open/open configuration and provide a parametric study of their range of existence as a function of the parameters Re , β , M .

[Figure 11\(a\)](#) displays the range of existence of instabilities as a function of Re and β for three values of M . Two different modes, corresponding to the purely hydrodynamic modes H_2 and H_3 as identified by Fabre *et al.* (2020), are documented. Note that higher instability modes, called H_i with $i = 4, 5, 6 \dots$, exist in the studied interval of the parameter β ; however, they arise at larger values of Re and are not considered. The curves displayed in the figure for the smallest value of M , namely 10^{-2} , are very close to the predictions obtained by Fabre *et al.* (2020, figure 15), which is represented by dots in [figure 11](#). One can see that compressibility has almost no effect on the instability threshold of mode H_2 . On the other hand, it has a destabilizing effect on mode H_3 . [Figure 11\(b\)](#) investigates the effect of compressibility on the oscillation frequency, here represented as a Strouhal number $St_\beta = \omega_R \beta / 2\pi$. One can see that compressibility decreases the frequency for the shortest holes and has almost no effect on frequency for longer ones. This behaviour is associated with the significant modification of the threshold of instability (Re) for short holes (left asymptote of either H_2 or H_3 in [figure 11](#)), which does not occur for holes with a larger β value. A substantial variation in the critical Reynolds number induces a modification of the vena contracta coefficient α_{vena} (see, e.g. [figure 16](#)), which in turn may be linked to the frequency of the instability; see the discussion in [Appendix D](#).

6.2. Effect of Mach number – sensitivity analysis

In order to explain these observed trends, we consider the sensitivity $d\omega/dM$ of the complex frequency ω with respect to M . This quantity may be split into two terms, corresponding respectively to the sensitivity to base flow modifications and to the sensitivity to a Mach number variation of the linearized equations,

$$\left. \frac{d\omega}{dM} \right|_M = \left. \frac{\partial \omega}{\partial M} \right|_{q_0} + \left. \frac{\partial \omega}{\partial q_0} \right|_M \frac{\partial q_0}{\partial M}. \quad (6.1)$$

We have employed two techniques, a continuous adjoint technique described in Meliga, Sipp & Chomaz (2010) and a forward evaluation of the sensitivity. Provided the Mach number is close to the incompressible limit, the continuous adjoint technique provides

less accurate results; for this reason, we have decided to perform a forward evaluation. The first term $\partial\omega/\partial M$ is evaluated using a first-order finite difference, which requires the resolution of two eigenvalue problems (4.8) with the steady state frozen at the Mach number M , and with a Mach number perturbation of a small magnitude $\Delta M \ll M$ in the linearized Navier–Stokes operator of the eigenvalue problem. The second term is also evaluated by finite difference using two different steady states computed at M and $M + \Delta M$ where the Jacobian operator is evaluated at M . Figure 12 displays the sensitivity computed in such a way for a value of Re corresponding to the thresholds of the instability for modes H_2 (with $\beta = 0.8$) and H_3 (with $\beta = 2$). The figure also displays the value of $\partial\omega_1/\partial M$ obtained from the asymptotic model (3.12), which is a constant. Figure 12(a) reports a linear variation of the two terms of the sensitivity with respect to Mach number. A Mach number variation in the base flow has a stabilizing effect, whereas the instability is triggered by small variations of the Mach number of the linearized operator. The most dominant term for this kind of acoustically compact solutions seems to be the base flow effect, which has a small stabilizing effect. In particular, it explains the almost insignificant variation of the H_2 neutral curves in figure 11. Concerning the frequency, both terms have an almost opposite effect, which implies an almost null variation of the instability frequency for the H_2 mode. The impedance criterion in this case predicts a stabilizing effect with a small frequency increase, which holds relatively well for $M < 0.02$. On the other hand, the variation with respect to the Mach number of the growth rate and the frequency of instability of a configuration that is no longer acoustically compact for Mach numbers of the order of $M \sim 10^{-2}$ such as the H_3 mode at threshold for $\beta = 0.8$ greatly differs with the estimations made with the impedance criterion. Figure 12(b) reports a similar stabilizing effect of the base flow to the one of the H_2 mode. However, in this case variations of the Mach number in the linearized operator greatly destabilize the steady state, which causes the large variations in the neutral curves displayed in figure 11. In terms of frequency variations, it is possible to observe much larger excursions, which are negative and constant for $M < 0.07$ and increase linearly for $M > 0.07$. So we may conclude that the impedance criterion holds relatively well for large β and instability modes with low frequency, which are in turn the most acoustically compact, but it fails to predict accurate trends even for low Mach numbers for modes with higher frequencies and small length to thickness ratios.

6.3. Directivity of acoustic emission

Finally, we address the influence of parameters (β, M) on the directivity pattern of instabilities of type H_2 and H_3 . For that purpose, we evaluate the set of neutral eigenmodes for each pair (β, M) . Note that the amplitude of the eigenmodes are arbitrary, the pressure levels displayed in figure 14 have been normalized with respect to the monopole radiation (based on the oscillating volume flux through the perforation). Three values of the Mach number $M = \{10^{-2}, 2 \times 10^{-2}, 5 \times 10^{-2}\}$ and two of the dimensionless parameter $\beta = \{1, 2\}$ are selected for this study. The configuration $\beta = 1$ corresponds to a configuration less acoustically compact than $\beta = 2$ and it seems *a priori* more likely that the radiation differs from the single monopole pattern. Figure 13 displays the acoustic pressure levels of the real part of the neutral eigenmodes, H_2 in the upper part and H_3 in the lower part, for $M = 5 \times 10^{-2}$ and $\beta = 1$ (a) and $\beta = 2$ (b). Figure 13(a) displays the pressure levels in logarithmic scale for $\beta = 1$. In that figure one can appreciate a monopolar-like radiation for H_3 ; however, at $M = 5 \times 10^{-2}$ the H_2 mode displays a radiation pattern with a preferential direction aligned with the streamwise coordinate. In such a configuration,

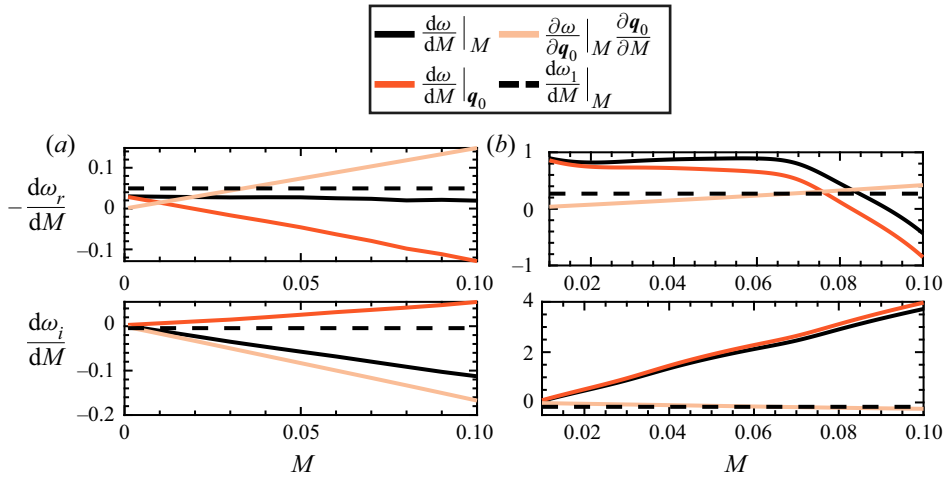


Figure 12. Sensitivity to Mach number variations of the complex frequency ω at the threshold of instability. Dashed line denotes the impedance estimation. (a) Mode H_2 for $\beta = 2$. (b) Mode H_3 for $\beta = 0.8$.

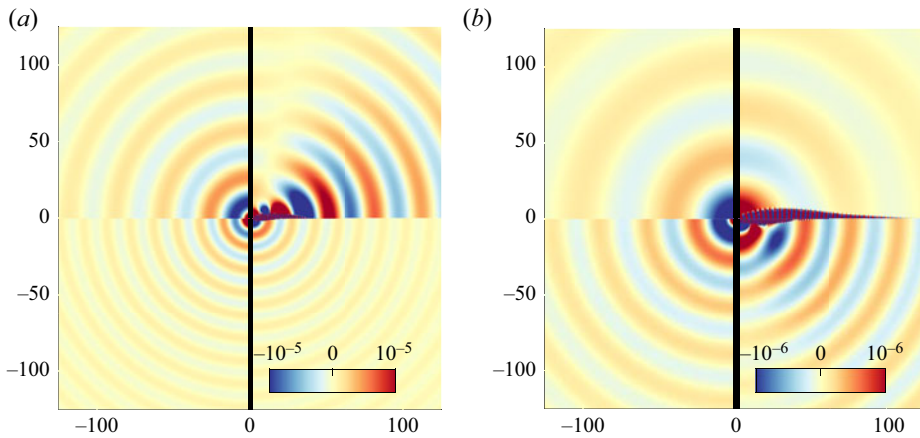


Figure 13. Real part of the pressure component of neutral eigenvalues H_2 (upper part) and H_3 (lower part) at $M = 5 \times 10^{-2}$; (a) $\beta = 1$ and (b) $\beta = 2$.

either the hole and the jet emit sound, which produces an uneven radiation of sound downstream and upstream of the hole. These observations can be better appreciated in [figure 14\(a\)](#), where the departures from an isotropic radiation for $M = 10^{-2}$ and the sound emission for $M = 5 \times 10^{-2}$ are clearly seen. For $\beta = 2$ ([figures 13\(b\)](#) and [14\(c\)](#)), the neutral eigenmodes display a fairly monopolar-like radiation; for the H_3 mode ([figure 14d](#)), higher pressure levels are measured downstream of the hole for directions forming an angle less than 45 degrees with the axis of symmetry.

7. Conclusion

The objective of the present paper was to investigate how the instability potential of a single jet passing through a hole in a thick plate, recently identified by Fabre *et al.* (2020) using LNSE in a strictly incompressible setting, manifests in a more realistic configuration involving compressibility. For this sake, we considered two generic situations. In the first

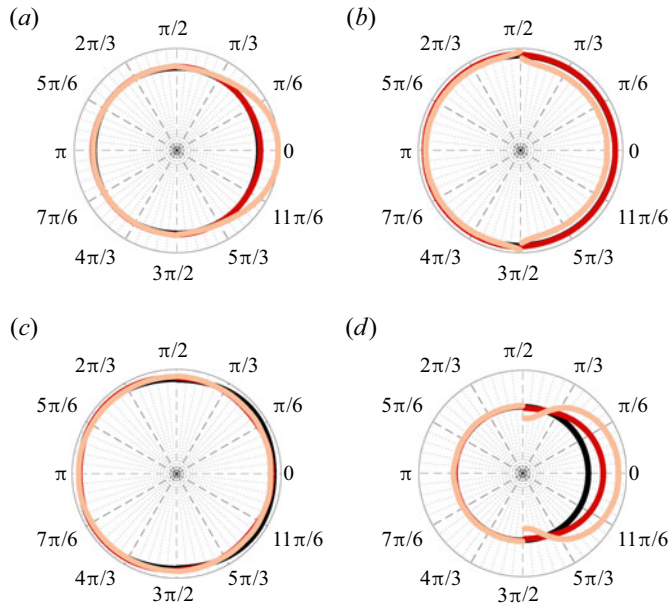


Figure 14. Directivity patterns, in logarithmic scale, measured at $r_x = \sqrt{r^2 + x^2} = 150$. Results are shown for (a) H_2 and $\beta = 1$; (b) H_3 and $\beta = 1$; (c) H_2 and $\beta = 2$; (d) H_3 and $\beta = 2$. Colour legend: (—, black) $M = 10^{-2}$, (—, red) $M = 2 \times 10^{-2}$ and (—, yellow) $M = 5 \times 10^{-2}$.

situation, the upstream domain is a closed cavity and the downstream domain is an open space. This situation was chosen to check the conditional instability mechanism, requiring the existence of a conveniently tuned resonator. In the second situation, the two regions, upstream and downstream of the hole, are considered as open. This situation was chosen to check the purely hydrodynamical instability which is expected to exist even in the absence of a resonator.

The two cases have been analysed with an asymptotic method, which provides an instability criterion and an estimate for the amplification rate. The method consists, in a first step, in writing an impedance of the global system incorporating the hole impedance as computed by Fabre *et al.* (2020) and modelling the impedance of the upstream and downstream regions, and in a second step, in performing a Taylor expansion of this impedance around the real ω -axis to identify its zeros. The great advantage of the method is that the Mach number M and the cavity volume V_{in} appear as parameters in the model, so that a parametric study of the problem can be done entirely in terms of the Reynolds number and aspect ratio, therefore reducing the number of computational parameters from four to two.

The potential to accurately predict the instability properties via the asymptotic model is put into test in §§ 5.3 and 6 for the conditional and pure hydrodynamic cases, respectively. A cross-comparison with the results carried out with the compressible Navier–Stokes equations shows a good match between the two approaches. The impedance criterion has been employed to identify the regions of existence in the (Re, χ) plane of a series of C_i , $i = 1, 2, 3, 4, \dots$ modes. In addition to these acoustically compact modes, at larger Reynolds numbers, there exist unstable modes associated with higher-order modes of the cavity connected upstream (see figure 7 for an example of that phenomenon). The use of the impedance criterion for the characterisation of the compressibility effect in the pure hydrodynamical case is less accurate. We have observed that the estimations of

the growth rate are relatively acceptable for the H_2 mode, but they are faulty for the H_3 mode, in particular for small length to diameter ratios. The inadequacy of the criteria to characterise this case can be attributed to the lack in the asymptotic model of the effect of the backward-travelling acoustic wave. These results suggest that a better modelling of the hydrodynamic-acoustic interaction is required to gain in accuracy. Finally, in § 6 we have examined the influence of the Mach number on the directivity pattern of the family of the pure hydrodynamical modes.

Declaration of interests. The authors report no conflict of interest.

Author ORCIDs.

 J. Sierra-Ausin <https://orcid.org/0000-0001-6036-5093>;

 D. Fabre <https://orcid.org/0000-0003-1875-6386>;

 V. Citro <https://orcid.org/0000-0003-2923-9157>;

 F. Giannetti <https://orcid.org/0000-0002-3744-3978>.

Appendix A. Computation of the hole impedance thanks to incompressible LNSE

A.1. Incompressible Navier–Stokes equations

Under the hypothesis of acoustic compactness, discussed in § 2.3, the flow is assumed to be locally incompressible in the region of the hole, where the fluid motion is governed by the incompressible Navier–Stokes equations

$$\frac{\partial}{\partial t} \begin{bmatrix} \mathbf{u} \\ 0 \end{bmatrix} = \mathcal{NS} \left(\begin{bmatrix} \mathbf{u} \\ p \end{bmatrix} \right) = \begin{bmatrix} -\mathbf{u} \cdot \nabla \mathbf{u} - \nabla p + Re^{-1} \nabla^2 \mathbf{u} \\ \nabla \cdot \mathbf{u} \end{bmatrix}. \quad (\text{A1})$$

The stability of the steady state $[\mathbf{u}_0, p_0]$ is investigated by using the linearized approach, in which the total flow field is decomposed into the sum of a steady base flow and a small time-harmonic perturbation as

$$\begin{bmatrix} \mathbf{u} \\ p \end{bmatrix} = \begin{bmatrix} \mathbf{u}_0 \\ p_0 \end{bmatrix} + \varepsilon \left(\begin{bmatrix} \hat{\mathbf{u}} \\ \hat{p} \end{bmatrix} e^{-i\omega t} + c.c. \right). \quad (\text{A2})$$

A.2. Incompressible Navier–Stokes equations – base-flow equations

The base flow is the solution of the steady version of the Navier–Stokes equations

$$\mathcal{NS}[\mathbf{u}_0; p_0] = 0, \quad (\text{A3})$$

with the following set of boundary conditions:

$$\int_{\Gamma_{in}} \mathbf{u}_0 \cdot \mathbf{n} \, dS = Q_0, \quad (\text{A4a})$$

$$p_0 = 0 \quad \text{on } \Gamma_{out}. \quad (\text{A4b})$$

This problem is solved using a classical Newton iteration.

A.3. Linearized incompressible Navier–Stokes equations – forced problem

The linear perturbation is governed by the equations

$$-i\omega \mathbf{B}[\hat{\mathbf{u}}, \hat{p}]^T = \mathbf{LNS}_0([\hat{\mathbf{u}}, \hat{p}]^T), \quad (\text{A5})$$

where \mathbf{LNS}_0 is the linearized Navier–Stokes operator around the base flow and \mathbf{B} is a weight operator defined as

$$\mathbf{LNS}_0 \begin{bmatrix} \hat{\mathbf{u}} \\ \hat{p} \end{bmatrix} = \begin{bmatrix} -(u_0 \cdot \nabla \hat{\mathbf{u}} + \hat{\mathbf{u}} \cdot \nabla u_0) - \nabla \hat{p} + Re^{-1} \nabla^2 \hat{\mathbf{u}} \\ \nabla \cdot \hat{\mathbf{u}} \end{bmatrix}; \quad \mathbf{B} = \begin{bmatrix} 1 & 0 \\ 0 & 0 \end{bmatrix}. \quad (\text{A6a,b})$$

Equation (A6a,b) is complemented with the following boundary conditions:

$$\int_{\Gamma_{in}} \hat{\mathbf{u}} \cdot \mathbf{n} \, dS = q', \quad (\text{A7})$$

$$\hat{p}(x, r) = 0 \quad \text{on } \Gamma_{out}. \quad (\text{A8})$$

A non-zero perturbation of the flow rate q' is imposed, fixed arbitrarily, to $q' = 1$. Equation (A7) thus leads to a non-homogeneous Dirichlet boundary condition at the inlet plane, treated by imposing a constant axial velocity \hat{u}_x . The problem can be symbolically written as

$$[\mathbf{LNS} + i\omega \mathbf{B}][\hat{\mathbf{u}}; \hat{p}] = \mathbf{F}, \quad (\text{A9})$$

where \mathbf{LNS} is the linearized Navier–Stokes operator (implicitly containing the homogeneous boundary condition at the outlet), and \mathbf{F} represents symbolically the non-homogeneous boundary condition at the inlet. This problem is non-singular and readily solved. Since \hat{p} has been set to zero (without loss of generality) along the outlet boundary, the pressure drop $p'_{in} - p'_{out}$ can be extracted from $[\hat{\mathbf{u}}; \hat{p}]$ by retrieving the mean value of the \hat{p} component along the inlet boundary Γ_{in} of the computational domain; such an operation can be written formally as $p'_{in} = \mathbf{P}[\hat{\mathbf{u}}, \hat{p}]$, where \mathbf{P} is a linear operator. The impedance is then ultimately deduced as $Z_h = \mathbf{P} \cdot (\mathbf{LNS} + i\omega \mathbf{B})^{-1} \cdot \mathbf{F}$.

Appendix B. Properties of the compressible steady state

As illustrated in figure 15, the base flow is characterised by a recirculation region originating from the upper corner of the hole. The pressure jump due to this recirculation can be represented by the so-called discharge coefficient (also called the vena contracta coefficient) $\alpha_{vena} = R_h^2/R_J^2$, where R_J is the effective radius of the jet. This function has been tabulated by Fabre *et al.* (2020) as a function of Re and β in the incompressible case. When taking into account the compressibility effects, the discharge coefficient (Bragg 1960) can be written in term of the dimensionless variables introduced in § 4.1 as

$$\alpha_{vena} = \frac{\dot{m}_0}{\pi R_h^2 \frac{1 + \gamma M^2 P_{in}}{\sqrt{T_{in}}} \frac{1}{M} \sqrt{\frac{2}{\gamma - 1} \left[\left(\frac{1 + \gamma M^2 P_{in}}{1 + \gamma M^2 P_{out}} \right)^{-2/\gamma} - \left(\frac{1 + \gamma M^2 P_{in}}{1 + \gamma M^2 P_{out}} \right)^{-(\gamma+1)/\gamma} \right]}}, \quad (\text{B1})$$

which in the low Mach number limit can be approximated as

$$\alpha_{vena} = \frac{\dot{m}_0}{\pi R_h^2 \sqrt{\rho_{in} (2(P_{in} - P_{out}) - 3M^2(P_{in} - P_{out})^2)}}, \quad (\text{B2})$$

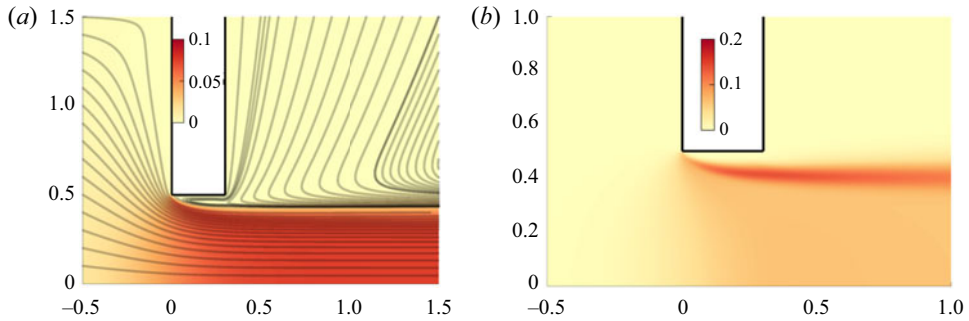


Figure 15. Contour plot of the base flow q_0 for $\beta = 0.3$, $Re = 1400$ and $M = 5 \times 10^{-2}$. (a) Spatial evolution of the Mach number. (b) Spatial evolution of the sensitivity of the axial velocity with respect to the Mach number $\nabla_M w_0$.

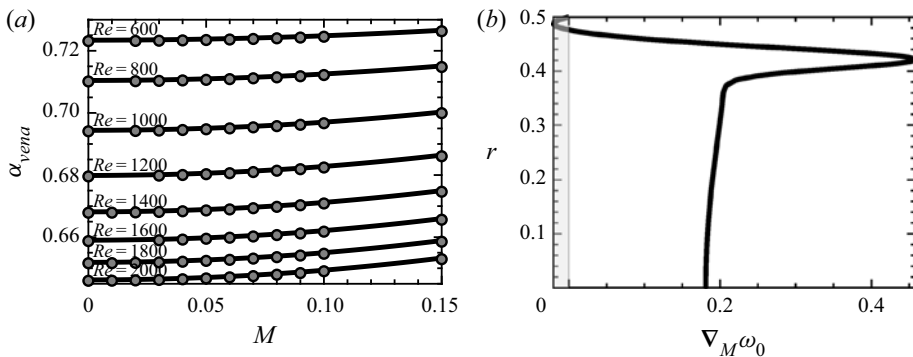


Figure 16. Discharge coefficient as a function of Mach number for several Re for $\beta = 0.3$. Dots correspond to computed values of α_{vena} , lines correspond to the theoretical estimation, cf. Bragg (1960). (b) Axial velocity profile of the sensitivity with respect to Mach number for $\beta = 0.3$, $Re = 1600$, $M = 10^{-1}$ at $z = 0.2$.

and it coincides with the one employed by Fabre *et al.* (2020) at the incompressible limit. Note that at large Reynolds numbers other simpler estimates exist, for instance, see the discussion by Gilbarg (1960) for the compressible Borda tube, which has been revisited by Durrieu *et al.* (2001) and compared against experimental evidence. Figure 16(a) displays the effect of the Mach number on the discharge coefficient. It shows a good quantitative agreement with the theoretical estimation, and it weakly increases with the Mach number. Compressibility effects accelerate the bulk flow within the jet core, whereas the flow within the recirculation region hardly changes (see the evolution of the sensitivity with respect to the Mach number of the streamwise velocity in figures 16(b) and 15(b)). In addition, it has been observed that the shear layer thickness remains unchanged with a weak Mach number increase ($M < 0.2$). In § 6 it is shown that an increase of the Mach number in the steady-state solution has a stabilizing effect, which can be attributed to an attenuated recirculation region.

Appendix C. Nyquist curve – Cauchy’s argument principle

Let us review the use of the Nyquist criterion together with the drawing of Nyquist curves. In the absence of poles in the real axis, the Nyquist plot is drawn along the real axis. However, in the presence of a pole of the impedance in the real axis, one

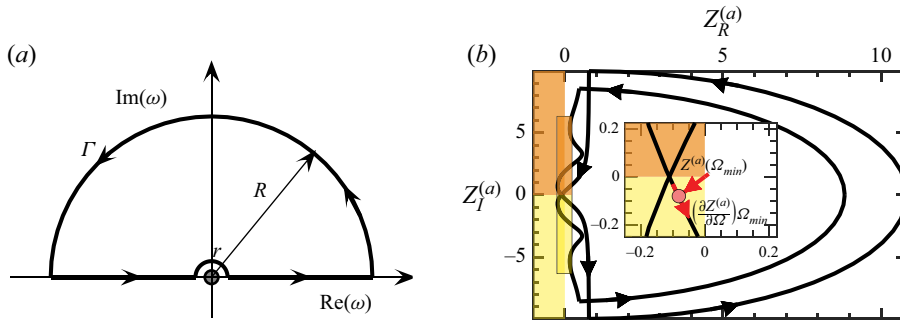


Figure 17. (a) The complex contour Γ of integration enclosing the unstable complex plane, where Cauchy's argument principle is applied. (b) Nyquist curve for the augmented system impedance along Γ .

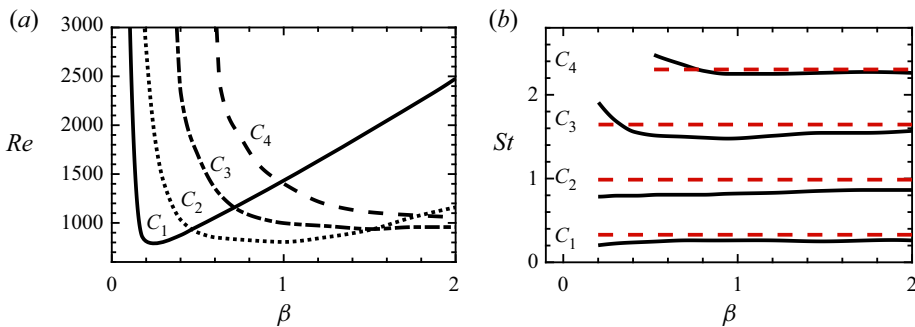


Figure 18. (a) Thresholds of the conditional instabilities C_1 , C_2 , C_3 and C_4 as a function of β and Re . (b) Strouhal evolution with β . Solid lines are the boundaries of the conditional stability computed with incompressible LNSE and dashed lines are the estimation with $\alpha_{vena} = 0.76$.

must take a contour that does not encircle the pole. In particular, the augmented system impedance possess a pole at $\omega = 0$, therefore, a complex contour that does not encircle zero is employed as the one depicted in figure 17(a). In the evaluation of the impedance, let us consider here without loss of generality the augmented system impedance $Z^{(a)}$ (either $Z^{(a)} = Z_a$ or $Z^{(a)} = Z_b$) along the contour Γ , i.e. $Z^{(a)}(\Gamma)$, which provides a direct evaluation of the stability of the system. Provided that the contour of integration does not encircle any pole of the system, which is satisfied by construction, the number of times that the curve $Z^{(a)}(\Gamma)$ encircles the origin in the counterclockwise direction determines the number of zeros in the area surrounded by the contour Γ . In the condition that the contour of integration Γ encloses the unstable complex plane, then any encirclement of the origin implies that the system is unstable. To illustrate this, let us consider the Nyquist curve represented in figure 17(b), where the curve $Z^{(a)}(\Gamma)$ is oriented counterclockwise, and it encircles twice the origin: this implies that the system has two unstable zeros. A more careful evaluation reveals that this corresponds to a pair of conjugated complex zeros.

Additionally, impedance values for real ω can also provide an estimation of the complex zeros whenever $\text{Im}(\omega)$ is of small magnitude. Here, let us detail the procedure followed in § 3.3.1. We consider the case where the Nyquist curve is found near the origin. The first scenario corresponds to a complex frequency $\omega = \omega_R + i\omega_I = \omega_0 + \varepsilon\omega_1$, where $\omega_0, \omega_R, \omega_I$ are real values, ω_1 is considered to be complex and a small real parameter $\varepsilon \ll 1$.

Provided the impedance $Z^{(a)}(\omega) = \text{Re}(Z^{(a)}(\omega)) + i\text{Im}(Z^{(a)}(\omega)) = Z_R^{(a)}(\omega) + iZ_I^{(a)}(\omega)$ is analytic, the first-order Taylor expansion at ω_0 provides

$$0 = Z^{(a)}(\omega) = Z^{(a)}(\omega_0) + \left(\frac{dZ^{(a)}}{d\omega} \right)_{\omega=\omega_0} (\omega - \omega_0) + R_1(\omega), \quad (\text{C1})$$

where $R_1(\omega)$ is the remainder of the Taylor expansion. The remainder of the expansion can be shown to be bounded, for instance, using Cauchy's integral formula and the maximum principle (see, for instance, Rudin 1987) yields

$$|R_1(\omega)| \leq M_r \frac{|\omega - \omega_0|^2}{r(r - |\omega - \omega_0|)} \leq M_r \frac{\eta^2}{1 - \eta}, \quad \text{with } M_r \equiv \max_{|\omega - \omega_0|=r} |Z^{(a)}(\omega)| \quad (\text{C2})$$

for $|\omega - \omega_0| < r$ and $|\omega - \omega_0|/r \leq \eta < 1$, where we have assumed that the impedance function is holomorphic in a closed disk of radius r of the complex plane. Therefore, the function $R_1(\omega)/(\omega - \omega_0)$ is also analytic within the disk. In such a way we can approximate the value of zero ω as

$$\begin{aligned} \omega - \omega_0 &= \frac{Z^{(a)}(\omega_0)}{\left(\frac{dZ^{(a)}}{d\omega} \right)_{\omega=\omega_0} + \frac{R_1(\omega)}{\omega - \omega_0}} \approx \frac{Z^{(a)}(\omega_0)}{\left(\frac{dZ^{(a)}}{d\omega} \right)_{\omega=\omega_0}} \\ &= \frac{Z_R^{(a)}(\omega_0) + iZ_I^{(a)}(\omega_0)}{\left(\frac{\partial Z_R^{(a)}(\omega)}{\partial \omega_R} \right)_{\omega=\omega_0} + i \left(\frac{\partial Z_I^{(a)}(\omega)}{\partial \omega_R} \right)_{\omega=\omega_0}}, \end{aligned} \quad (\text{C3})$$

where the error of the approximation is

$$\epsilon \leq \left| \frac{Z(\omega_0)}{\left(\frac{dZ}{d\omega} \right)_{\omega=\omega_0}} \right| \frac{\eta'}{1 - \eta'}, \quad (\text{C4})$$

with $\eta' = |R_1(\omega)|/|\omega - \omega_0|/|(dZ/d\omega)_{\omega=\omega_0}|$, because the radius of convergence of the rational complex function $1/((dZ/d\omega)_{\omega=\omega_0} + z)$ is equal to $|(dZ/d\omega)_{\omega=\omega_0}|$. Thus, the approximation (C3) converges uniformly far from the critical points of the impedance. Furthermore, it provides good estimates whenever $|Z(\omega_0)| \sim \varepsilon \ll 1$ and $|\omega - \omega_0| \sim \varepsilon \ll 1$, which is the motivation to the condition (i) and the expansion in frequency in § 3.3.1. Finally, note that (C3) could be used as a step in a Newton iteration, whenever the initial guess ω_0 is far from the zero of the impedance.

Multiplication by the complex conjugate of the denominator in (C3) leads to

$$\varepsilon \omega_1 \approx \frac{(Z_R^{(a)}(\omega_0) + iZ_I^{(a)}(\omega_0)) \left(\left(\frac{\partial Z_R^{(a)}(\omega)}{\partial \omega_R} \right)_{\omega=\omega_0} - i \left(\frac{\partial Z_I^{(a)}(\omega)}{\partial \omega_R} \right)_{\omega=\omega_0} \right)}{\left(\left(\frac{\partial Z_R^{(a)}(\omega)}{\partial \omega_R} \right)_{\omega=\omega_0} \right)^2 + \left(\left(\frac{\partial Z_I^{(a)}(\omega)}{\partial \omega_R} \right)_{\omega=\omega_0} \right)^2}. \quad (\text{C5})$$

Finally, one could split (C5) in real and imaginary parts, this yields the expression for ω_R ,

$$\varepsilon \text{Re}(\omega_1) = \omega_R - \omega_0 \approx \frac{\left(Z_R^{(a)}(\omega_0) \left(\frac{\partial Z_R^{(a)}(\omega)}{\partial \omega_R} \right)_{\omega=\omega_0} + Z_I^{(a)}(\omega_0) \left(\frac{\partial Z_I^{(a)}(\omega)}{\partial \omega_R} \right)_{\omega=\omega_0} \right)}{\left(\left(\frac{\partial Z_R^{(a)}(\omega)}{\partial \omega_R} \right)_{\omega=\omega_0} \right)^2 + \left(\left(\frac{\partial Z_I^{(a)}(\omega)}{\partial \omega_R} \right)_{\omega=\omega_0} \right)^2}, \quad (\text{C6})$$

and for ω_I ,

$$\varepsilon \text{Im}(\omega_1) = \omega_I \approx \frac{\left(Z_I^{(a)}(\omega_0) \left(\frac{\partial Z_R^{(a)}(\omega)}{\partial \omega_R} \right)_{\omega=\omega_0} - Z_R^{(a)}(\omega_0) \left(\frac{\partial Z_I^{(a)}(\omega)}{\partial \omega_R} \right)_{\omega=\omega_0} \right)}{\left(\left(\frac{\partial Z_R^{(a)}(\omega)}{\partial \omega_R} \right)_{\omega=\omega_0} \right)^2 + \left(\left(\frac{\partial Z_I^{(a)}(\omega)}{\partial \omega_R} \right)_{\omega=\omega_0} \right)^2}. \quad (\text{C7})$$

Appendix D. Frequency selection argument

This appendix provides an argument explaining the quantification of the eigenvalues observed for the cavity/open configuration.

The frequency of the sound generated is selected by considering the two elements that compose the feedback loop of a class III aerodynamic whistle: the hydrodynamic-acoustic wave interaction and the acoustic resonator. In this kind of mechanism, we can distinguish two feedback loops, a first loop composed of the interaction of a hydrodynamic instability with an acoustic wave and a second one which accounts for the interaction of the first feedback loop with the acoustic resonator. A hydrodynamic-acoustic wave interaction develops whenever the shear layer of the jet is unstable and the jet acts as a source of energy, which occurs when the resistance of the hole is negative. The shear layer instability is triggered at the leftmost corner of the hole, disturbances grow along the hole; however, in the case when the shear layer is not sufficiently unstable (so self-sustained oscillations arise by pure hydrodynamical arguments) it requires an acoustic wave to close the loop, which is an instantaneous process in the low Mach number limit. For acoustically compact source regions, the frequency selection of this mechanism is dominated by the hydrodynamic instability, because the travel time of the acoustic wave is of lower order of magnitude. Secondly, the cavity acts a resonator, selecting a set of discrete frequencies among those associated with a negative resistance.

In the present configuration, there exist four branches of instability, each of them denoted as C_n for $n = 1, 2, 3, 4$, which are characterised by a nearly constant Strouhal number

$$St_\beta^{(n)} = \frac{\omega^{(n)} \beta}{2\pi} \quad (\text{D1})$$

as β is varied. The characteristic frequency of C_n branches is related by a frequency shift $St_\beta^{(n)} = St_\beta^{(n-1)} + \Delta St_\beta$, where $\Delta St_\beta \approx [0.6, 0.7]$. This frequency shift may be estimated if one realizes that the global instability is the result of the constructive interaction

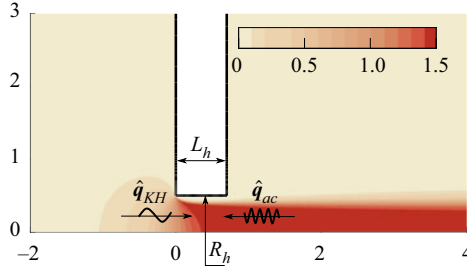


Figure 19. Diagram of the non-local interaction leading to global instability.

between two travelling waves: a downstream-travelling wave, which is excited about the hole lip and propagates around the jet core position, and an upstream-travelling wave that propagates backwards. The non-local constructive interaction of such waves gives rise to a self-sustained global in time instability, which, in some circumstances, is able to radiate an intense acoustic field.

In the following analysis we reconsider the discharge coefficient $\alpha_{vena} = \sqrt{\rho U_M^2 / 2(P_{in} - P_{out})}$, which can be thought of as a measure of the vena contracta phenomenon, assuming that the jet contracts to a top-hat jet with constant velocity U_J and radius R_J . Then applying Bernoulli law, one obtains $\alpha_{vena} = U_M / U_J = \pi R_J^2 / \pi R_h^2$ that was introduced in Fabre *et al.* (2019) in the discussion of the work of Howe (1979), which is classically associated with the pressure loss across the aperture, and it relates the mean velocity U_M with the jet velocity U_J . In Fabre *et al.* (2019, § 2.5 and Appendix A) the importance of the vena contracta coefficient α_{vena} and the actual value of the phase velocity of the Kelvin–Helmholtz instability, where the phase velocity depends on the frequency ω but which is around $U_c = U_J/2$ for sufficiently high ω . The value of the discharge coefficient tends asymptotically to $\alpha_{vena} \rightarrow 0.61$ for large Re ; however, in the range of Reynolds numbers where transition occurs α_{vena} is maximal and takes values $\alpha_{vena} \in [0.7, 0.76]$. In the following, we consider a constant discharge coefficient $\alpha_{vena} = 0.76$, which was the value reported in Fabre *et al.* (2020, figure 5) for most of β in the range of Reynolds numbers where the transition occurs.

In order to estimate the frequency shift ΔSt_β let us consider the travel time of each travelling wave past the hole. The hydrodynamic travelling wave takes $\Delta\tau_{KH} = L_h / U_c = 2\alpha_{vena} L_h / U_M$ and the acoustic wave $\Delta\tau_{ac} = M L_h / U_M$; therefore, the total travelling time

$$\Delta\tau = \Delta\tau_{KH} + \Delta\tau_{ac} = \frac{L_h(2\alpha_{vena} + M)}{U_M} \approx 2\alpha_{vena} \frac{L_h}{U_M}, \quad f^{(n)} = \frac{2n-1}{2\Delta\tau}, \quad \Delta f = \frac{1}{\Delta\tau}, \quad (D2a-c)$$

where it is considered that $M \ll 1$ and the convective velocity of the hydrodynamic perturbation is $\frac{2\alpha_{vena}}{U_M}$ as it is displayed in figure 19. Thus, the associated Strouhal shift

$$\Delta St_\beta = \frac{\Delta f L_h}{U_M} \approx \frac{1}{2\alpha_{vena}}. \quad (D3)$$

Similarly, the Strouhal frequency of each C_n branch is estimated as

$$St_\beta^{(n)} = \frac{2n-1}{4\alpha_{vena}}, \quad n = 1, 2, 3, \dots \quad (D4)$$

In the previous reasoning, it has been implicitly assumed that only odd mode structures as those depicted in Fabre *et al.* (2020, figure 9) lead to a conditional instability.

The superposition of the base flow with odd modes (respectively even) at the instant of the cycle where the flow rate through the hole is maximum results in an upward (respectively downward) displacement of the shear layer, thus, pressure is increased (respectively decreased) in the presence of odd modes (respectively *even*). This implies that the hole impedance is negative, which is the criterion of existence of conditional stability.

Finally, let us discuss the influence of compressibility regarding modifications in frequency at the threshold of instability for each of the unstable modes. Compressibility induces a weak variation in the vena contracta coefficient, see [figure 16\(a\)](#), while the threshold of instability is significantly modified for a given value of β near the left asymptote for conditional instabilities ([figure 18a](#)) and hydrodynamic instabilities ([figure 11a](#)). Thus, for short holes β (here short refers to a value of β near a vertical asymptote of the corresponding instability), the critical Reynolds number is considerably modified by compressible effects, which in turn induces a change in the vena contracta coefficient (more important than the variation of the vena contracta by compressibility at constant Reynolds number). For those cases, one could evaluate the shift in frequency $\delta|_M \Delta St_\beta = \Delta St_\beta(M + \Delta M) - \Delta St_\beta(M)$ as

$$\delta|_M \Delta St_\beta = - \frac{2(\alpha_{vena}(Re_c(M + \Delta M), M + \Delta M) - \alpha_{vena}(Re_c(M), M)) + \Delta M}{(2\alpha_{vena}(Re_c(M), M) + M)^2}, \quad (D5)$$

where the first term, the variation in the vena contracta due to a variation in Mach number, is negligible with respect to the variation in Mach number for long holes, and thus, the variation of frequency for those instabilities is of lesser importance.

Appendix E. Computational domains and absorbing boundary layer

This section discusses the design of computational domains used for the computation of steady states and eigenmodes with the full compressible formulation, and steady states and the forced harmonic response with the incompressible formulation. The computational strategy must be designed in such a way as to avoid the presence of spurious eigenvalues/eigenmodes. The creation of meshes for the full compressible formulation follows a block-structured strategy, similar to the one sketched in [figure 4](#). The domain is divided into three regions: an inner region with the highest vertex density, a mid region with intermediate vertex density and a coarser region for the absorbing layer. Meshes employed for the incompressible case are composed of two regions, a physical domain with the highest vertex density and a coarser region for the absorbing layer. [Table 1](#) lists a number of computational meshes employed in this study ($\mathbb{M}_2, \mathbb{M}_3, \mathbb{M}_4$ and \mathbb{M}_5 for the full compressible case, and \mathbb{M}_1 for the incompressible case). However, such a list is not exhaustive because in addition to the block-strategy refinement, the computational domain has been locally refined following an adaptive local refinement procedure, where the metric for the refinement is based on the steady state and on the eigenmodes (respectively steady state and forced harmonic response in the incompressible case), cf. Hecht (2012) and Fabre *et al.* (2018).

The absorbing boundary layer corresponds to the complex mapping technique (Sierra *et al.* 2020) where a coordinate transformation \mathcal{G} is defined as follows:

$$\left. \begin{aligned} \mathcal{G}_z : \mathbb{R} &\rightarrow \mathbb{C} \quad \text{such that } z = \mathcal{G}_z(Z) = [1 + i\gamma_{z,c}g_z(Z)]Z, \\ \mathcal{G}_r : \mathbb{R} &\rightarrow \mathbb{C} \quad \text{such that } r = \mathcal{G}_r(R) = [1 + i\gamma_{r,c}g_r(R)]R. \end{aligned} \right\} \quad (E1)$$

Here $g_z(Z)$ (respectively $g_r(R)$) has to be chosen as a smooth function such as $g_z(Z) = 0$ for $Z < Z_0$ and $g_z(Z) \approx 1$ for $Z > Z_0 + L_c$ up to Z_{max} . The complex mapping acts on

	Z_{max}	R_{max}	Z_0	L_c	$\gamma_{z,c}$	R_0	R_c	$\gamma_{r,c}$	n_{tri}
\mathbb{M}_1	50	50	10	2.5	0.3	5	2.5	0.3	42 460 tri.
\mathbb{M}_2	300	300	10	5	0.3	10	2.5	0.3	165 841 tri.
\mathbb{M}_3	600	600	10	5	0.3	10	2.5	0.3	235 874 tri.
\mathbb{M}_4	600	600	170	5	0.3	170	5	0.3	314 525 tri.
\mathbb{M}_5	1500	1500	10	5	0.3	10	2.5	0.3	413 356 tri.

Table 1. Meshes used for cases where the complex mapping technique is adopted. Note: the smooth transition functions are defined as $g_z(Z) = \tanh([(Z - Z_0)/L_c]^2)$ and $g_r(R) = \tanh([(R - R_0)/R_c]^2)$. In the following, $L_{max} = z_{-\infty} + z_{CM} = z_{\infty} + z_{CM}$ and $R_{max} = r_{\infty} + r_{CM}$ (figure 4).

a finite region of length $z_{CM} = Z_{max} - (Z_0 + L_c)$. The function g_z is defined as $g_z(Z) = \tanh([(Z - Z_0)/L_c]^2)$. The application of this map to the linearized Navier–Stokes requires that each spatial derivative, within the complex mapped region, is modified as

$$\frac{\partial}{\partial z} \equiv \mathcal{H}_z \frac{\partial}{\partial Z} \quad \text{with } \mathcal{H}_z(Z) = \left(\frac{\partial g_z}{\partial Z} \right)^{-1}. \quad (\text{E2})$$

An example of parameters for the usage of the complex mapping layer for the incompressible case is listed in table 1 (\mathbb{M}_1). In the full compressible formulation, one must pay particular attention to the extension of the complex mapping region, which here is selected to cover at least two acoustic wavelengths, i.e. $z_{CM} = r_{CM} > 1/StM$. For instance, the largest acoustic wavelength in this study corresponds to the validation case in § 5.1, where $\lambda_{ac} \approx 600$ ($St \approx 1/3$ and $M = 5 \times 10^{-3}$), for which \mathbb{M}_5 is an appropriate choice.

REFERENCES

- ANDERSON, A.B.C. 1954 A jet-tone orifice number for orifices of small thickness-diameter ratio. *J. Acoust. Soc. Am.* **26** (1), 21–25.
- BOUASSE, H. 1929 *Instruments à vent*. Impr. Delagrave.
- Bragg, S.L. 1960 Effect of compressibility on the discharge coefficient of orifices and convergent nozzles. *J. Mech. Engng Sci.* **2** (1), 35–44.
- CASTELLENGO, M. 1999 Acoustical analysis of initial transients in flute like instruments. *Acta Acust. United Acust.* **85** (3), 387–400.
- CHANAUD, R.C. 1970 Aerodynamic whistles. *Sci. Am.* **222** (1), 40–47.
- COLTMAN, J.W. 1976 Jet drive mechanisms in edge tones and organ pipes. *J. Acoust. Soc. Am.* **60** (3), 725–733.
- DAI, X. & AURÉGAN, Y. 2016 Acoustic of a perforated liner with grazing flow: Floquet-Bloch periodical approach versus impedance continuous approach. *J. Acoust. Soc. Am.* **140** (3), 2047–2055.
- DAI, X. & AURÉGAN, Y. 2018 A cavity-by-cavity description of the aeroacoustic instability over a liner with a grazing flow. *J. Fluid Mech.* **852**, 126–145.
- DURRIEU, P.P.J.M., HOFMANS, G., AJELLO, G., BOOT, R., AURÉGAN, Y., HIRSCHBERG, A. & PETERS, M.C.A.M. 2001 Quasisteady aero-acoustic response of orifices. *J. Acoust. Soc. Am.* **110** (4), 1859–1872.
- ELDRIDGE, J.D. & DOWLING, A.P. 2003 The absorption of axial acoustic waves by a perforated liner with bias flow. *J. Fluid Mech.* **485**, 307–335.
- FABRE, D., CITRO, V., FERREIRA, D., BONNEFIS, P., SIERRA, J., GIANNETTI, F. & PIGOU, M. 2018 A practical review on linear and nonlinear global approaches to flow instabilities. *Appl. Mech. Rev.* **70** (6), 060802.
- FABRE, D., LONGOBARDI, R., BONNEFIS, P. & LUCHINI, P. 2019 The acoustic impedance of a laminar viscous jet through a thin circular aperture. *J. Fluid Mech.* **864**, 5–44.
- FABRE, D., LONGOBARDI, R., CITRO, V. & LUCHINI, P. 2020 Acoustic impedance and hydrodynamic instability of the flow through a circular aperture in a thick plate. *J. Fluid Mech.* **885**, A11.
- FERREIRA SABINO, D., FABRE, D., LEONTINI, J. & LO JACONO, D. 2020 Vortex-induced vibration prediction via an impedance criterion. *J. Fluid Mech.* **890**, A4.

- FLETCHER, N.H. & ROSSING, T.D. 2012 *The Physics of Musical Instruments*. Springer Science & Business Media.
- GILBARG, D. 1960 Jets and cavities. In *Fluid Dynamics/Strömungsmechanik* (ed. S. Flügge), pp. 311–445. Springer.
- HECHT, F. 2012 New development in freefem++. *J. Numer. Maths* **20** (3–4), 251–266.
- HENRYWOOD, R.H. & AGARWAL, A. 2013 The aeroacoustics of a steam kettle. *Phys. Fluids* **25** (10), 107101.
- HEUWINKEL, C., ENGHARDT, L. & ROHLE, I. 2007 Experimental investigation of the acoustic damping of perforated liners with bias flow. In *13th AIAA/CEAS Aeroacoustics Conference (28th AIAA Aeroacoustics Conference)*, AIAA Paper 2007-3525.
- HOWE, M.S. 1979 On the theory of unsteady high Reynolds number flow through a circular aperture. *Proc. R. Soc. Lond. A* **366** (1725), 205–223.
- HUGHES, I.J. & DOWLING, A.P. 1990 The absorption of sound by perforated linings. *J. Fluid Mech.* **218**, 299–335.
- JING, X. & SUN, X. 2000 Effect of plate thickness on impedance of perforated plates with bias flow. *AIAA J.* **38** (9), 1573–1578.
- LONGOBARDI, R., FABRE, D., BONNEFIS, P., CITRO, V., GIANNETTI, F. & LUCHINI, P. 2021 Studying sound production in the hole-tone configuration using compressible and incompressible global stability analyses. In *Advances in Critical Flow Dynamics Involving Moving/Deformable Structures with Design Applications: Proceedings of the IUTAM Symposium on Critical Flow Dynamics involving Moving/Deformable Structures with Design applications* (ed. M. Braza, K. Hourigan & M. Triantafyllou), pp. 251–263. Springer.
- MELIGA, P., SIPP, D. & CHOMAZ, J.-M. 2010 Effect of compressibility on the global stability of axisymmetric wake flows. *J. Fluid Mech.* **660**, 499–526.
- MOUSSOU, P., TESTUD, P., AUREGAN, Y. & HIRSCHBERG, A. 2007 An acoustic criterion for the whistling of orifices in pipes. In *ASME Pressure Vessels and Piping Conference*, vol. 42827, pp. 345–353.
- PIERCE, A.D. 2019 *Acoustics: An Introduction to its Physical Principles and Applications*. Springer.
- ROSSING, T.D. 2007 *Springer Handbook of Acoustics*, vol. 1. Springer.
- RUDIN, W. 1987 *Complex and real Analysis*. McGraw Hill Book Co.
- RUPP, J., CARROTTE, J. & MACQUISTEN, M. 2012 The use of perforated damping liners in aero gas turbine combustion systems. *Trans. ASME J. Engng Gas Turbines Power* **134** (7), 071502.
- SIERRA, J., FABRE, D. & CITRO, V. 2020 Efficient stability analysis of fluid flows using complex mapping techniques. *Comput. Phys. Commun.* **251**, 107100.
- SU, J., RUPP, J., GARMORY, A. & CARROTTE, J.F. 2015 Measurements and computational fluid dynamics predictions of the acoustic impedance of orifices. *J. Sound Vib.* **352**, 174–191.
- VERGE, M.-P., HIRSCHBERG, A. & CAUSSE, R. 1997 Sound production in recorderlike instruments. II. A simulation model. *J. Acoust. Soc. Am.* **101** (5), 2925–2939.